Diplomarbeit

Supernova Detection in a future Extension of the IceCube Neutrino Telescope

Lukas Schulte

14. Juni 2011

Institut für Physik
Johannes Gutenberg-Universität Mainz

Supernova Detection in a future Extension of the IceCube Neutrino Telescope

Erster Gutachter: Name gelöscht
Zweiter Gutachter: Name gelöscht

Marking the final explosive burning stage of massive stars, supernovae are one the of most energetic celestial events. Apart from their enormous optical brightness they are also known to be associated with strong emission of MeV neutrinos—up to now the only proven source of extrasolar neutrinos.

Although being designed for the detection of high energy neutrinos, the recently completed IceCube neutrino telescope in the antarctic ice will have the highest sensitivity of all current experiments to measure the shape of the neutrino light curve, which is in the MeV range. This measurement is crucial for the understanding of supernova dynamics.

In this thesis, the development of a Monte Carlo simulation for a future low energy extension of IceCube, called PINGU, is described that investigates the response of PINGU to a supernova. Using this simulation, various detector configurations are analysed and optimised for supernova detection. The prospects of extracting not only the total light curve, but also the direction of the supernova and the mean neutrino energy from the data are discussed. Finally the performance of PINGU is compared to the current capabilities of IceCube.

Supernovae, die letzte, explosive Brennphase massereicher Sterne, stellen eines der energiereichsten Ereignisse dar, die man im Universum beobachten kann. Neben ihrer enormen Leuchtkraft sind sie bekanntermaßen auch mit einer starken Emission von Neutrinos im MeV-Bereich verbunden – und bislang die einzige nachgewiesene Neutrinoquelle außerhalb des Sonnensystems.

Obwohl es für den Nachweis hochenergetischer Neutrinos ausgelegt ist, weist das kürzlich fertig gestellte Neutrinoteleskop IceCube im antarktischen Eis im Fall einer galaktischen Supernova die höchste Sensitivität aller derzeit laufenden Experimente für ihre Neutrino-Lichtkurve auf, die im MeV-Bereich liegt. Deren Kenntnis ist entscheidend für das Verständnis der Dynamik von Supernovae.

In dieser Arbeit wird die Entwicklung einer Monte-Carlo-Simulation für eine zukünftige Niederenergieerweiterung von IceCube, genannt PINGU, beschrieben, die die Reaktion von PINGU auf eine Supernova modelliert. Mit dieser Simulation werden verschiedene Detektorkonfigurationen untersucht und für den Supernova-Nachweis optimiert. Die Möglichkeiten, neben der integralen Lichtkurve auch die Richtung der Supernova sowie die mittlere Neutrinoenergie aus den Daten zu bestimmen, werden diskutiert. Schließlich wird die Fähigkeit von PINGU zum Nachweis von Supernovae mit der von IceCube in der jetzigen Konfiguration verglichen.

Contents

1 Theory

In this chapter, the underlying physics that form the basis of this thesis will be discussed in detail. The focus is laid on the physics of neutrinos and their detection as well as on the stellar evolution and the physics of supernovae.

1.1 Neutrinos and their Interactions

1.1.1 Neutrinos in the Standard Model

The Standard Model of Particle Physics

The standard model of particle physics is the combination of the current theories of the electroweak and strong interactions. It has been very successful since it was established during the 1970s. Up to now no experiments have shown results that are in clear disagreement with the standard model, although the search for so called "new physics" has been the major topic in particle physics for the last years and many extensions of it have been discussed.

The standard model is a quantum field theory of the three fundamental forces which are relevant on scales that are accessible for particle physics. Each of these forces is represented by one or more exchange bosons with spin 1 that couple to the according charge. Formally, the bosons are the generators of the gauge symmetry group of the particular interaction.

So the strong force, which has a $SU(3)$ symmetry and therefore eight generators, is transmitted by the eight gluons which couple to the "colour" charge. It has the largest coupling constant and so it is dominant whenever the strong interaction is allowed. However, as the colour charge is "confined", i. e. colour must not be visible from outside, and the gluons are coloured themselves and hence self-coupling, the range of the strong interaction is limited to about the size of a nucleus.

The electromagnetic coupling is about two orders of magnitude weaker than the strong one, but not restricted in range. This is due to the fact that its one exchange boson, the photon, which couples to the electrical charge, is massless and shows no self-interaction. Also, there is no confinement on the charge, which is the reason why electromagnetic phenomena can be observed on macroscopic scales.

For low energies, the effective coupling constant of the weak interaction lies another three orders of magnitude below the electromagnetic one. The three exchange

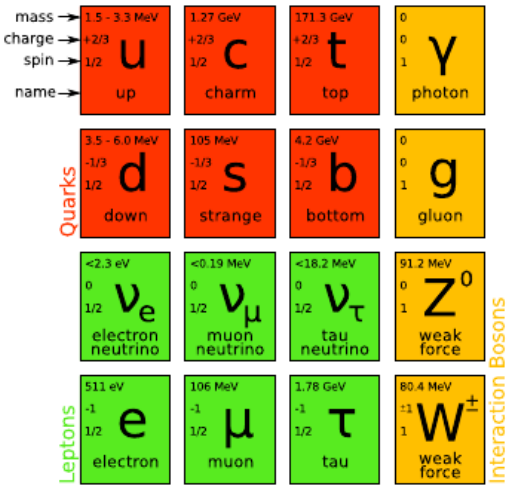

Figure 1.1: Fundamental particles in the standard model of particle physics. Values taken from [44]

bosons originating from its $SU(2)$ symmetry are the $W^{\pm}$ and Z^0 bosons, whose masses of about 90 MeV limit its range to the subatomic scale. However, as one can see from the fact that the weak interaction bosons are also electrically charged, electromagnetic and weak force are not completely separate. They can be unified to form one electroweak interaction which decomposes into two interactions via spontaneous symmetry breaking at lower energies. The breaking of the $SU(2)$ symmetry is also the mechanism by that the W and Z bosons gain their masses.

Apart from the exchange bosons, all particles that are currently known take part in the weak interaction. In most cases, however, weak reactions can be observed only if the strong and electromagnetic processes are suppressed.

The fourth known fundamental interaction, gravitation, is not part of the standard model due to the difficulties in formulating it as a quantum theory. Practically this is not a big problem as its coupling constant, the Newtonian gravitational constant, is more than 20 orders of magnitude smaller than the others and thus negligible for all energies that are currently accessible to quantum physics. On the other hand, electromagnetism and gravitation are unified as a non-quantum theory in special and general relativity. In principle, of course, it is one main goal in current-day physics to find a "theory of everything" which incorporates all known particles and interactions.

In addition to the spin 1 bosons, fermions with spin $\frac{1}{2}$ and their antiparticles form the second set of the particles within the standard model. They do not transmit any forces, but make up everything that is usually called "matter".

There are the six quarks u, d, c, s, t, and b, which obey all forces and—being coloured—are confined, so that no single quarks can be found in nature. Quarks are the constituents of baryons, like protons and neutrons, which consist of three quarks, and mesons consisting of a quark and an antiquark, like pions. Thus baryons and mesons, i. e. hadrons, are the only free particles that participate in the strong interaction although they are not coloured themselves, but contain coloured quarks.

The six remaining fundamental spin $\frac{1}{2}$ particles are called leptons and divided into the charged leptons e, μ, τ, and the three neutral neutrinos.

Properties of Neutrinos

Neutrinos are leptons and hence not strongly interacting, neither do they have an electrical charge. So the only way they can react with other particles is via weak processes, which is the reason why for a long time they were not expected to be detectable at all. By now, neutrinos can be detected in specially designed experiments and are in fact a subject of intense research.

As neutrinos are neither charged nor coloured, the remaining property one needs to determine is their mass. From radioactive beta decay, in which they were "seen" at first in the form of missing energy and momentum, one can only infer that the neutrino mass has to be very small, if not zero.

The fact that at least two neutrinos do have non-zero masses is implied by a phenomenon called neutrino oscillation. This effect occurs because the mass eigenstates of neutrinos, denoted by $|\nu_1\rangle$, $|\nu_2\rangle$, and $|\nu_3\rangle$, in which they propagate are different from the weak interaction eigenstates $|\nu_e\rangle$, $|\nu_\mu\rangle$, and $|\nu_\tau\rangle$, in which the neutrinos are created and undergo reactions.

If pure $|\nu_e\rangle$ are created, they propagate as a mixture of $|\nu_1\rangle$, $|\nu_2\rangle$, and $|\nu_3\rangle$. The fractions of the different mass eigenstates in this mixture changes during propagation as the propagators are mass dependent. If some distance away from the creation the neutrinos are detected, the mixture of mass eigenstates thus is different from the initial one, so that there is a non-zero probability to detect them as $|\nu_\mu\rangle$ or $|\nu_\tau\rangle$. A detailed description of neutrino oscillations with special focus on supernova neutrinos can be found in [35].

As neutrino oscillations could not happen if the mass eigenstates were degenerate, observing them does mean that there have to be at least two eigenstates with finite mass. Although there have been hints for neutrino oscillations since the late 1960's, their existence has been widely accepted only since 1998, when they were observed by the Kamiokande experiment [20, 23].

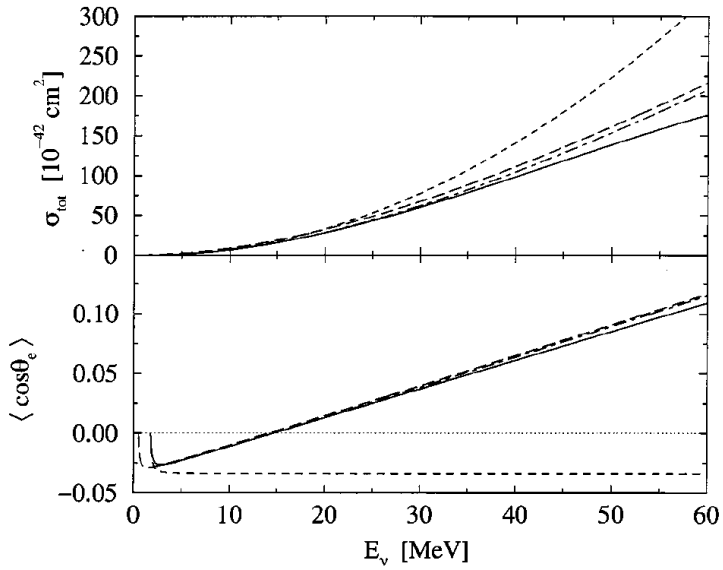

Figure 1.2: Total cross-section (top) and mean scattering angle (bottom) for inverse beta decay as a function of the antineutrino energy in different approximations. Graph taken from [58].

1.1.2 Interactions of Neutrinos in Ice

The polar ice, which is the medium for neutrino detection in the IceCube experiment, is very pure so that the contributions of anything else besides water molecules (like dust particles or frozen-in air) to the neutrino interaction cross-section can be neglected.

The ice itself provides three possible interaction partners for neutrinos: hydrogen (i. e. protons), oxygen nuclei, and electrons. All three react with neutrinos, but in very different strength. The "visible outcome" however is the same in all cases, namely a energetic positron or electron which emits Cherenkov light.

Inverse Beta Decay

Although this reaction is only available to electron anti-neutrinos, the inverse beta decay

$$\bar{\nu}_e + p \rightarrow n + e^+ \tag{1.1}$$

is the dominant channel for low-energy neutrino reactions in ice. Its cross-section is rather large (approximately given by $G_F^2 E_{\bar{\nu}_e}^2$, with G_F being the Fermi coupling constant) and well understood. Also, the energy threshold determined by kinematics

is very low,

$$E_{\bar{\nu}_e} \geq 1.806\,\mathrm{MeV} \approx (m_e + m_n) - m_p, \tag{1.2}$$

which makes it feasible for neutrinos with MeV energies that make up the signal expected from a supernova [57].

Due to the low threshold and the large mass difference between neutrino and proton on the one hand and positron and neutron on the other, the reaction is quasi-elastic, i. e. the neutrino energy is (after subtraction of the threshold) almost completely transferred to the positron. The difference between both can be fitted by

$$E_{\bar{\nu}_e} - E_{e^+} = \left[1.274 + 5.9 \cdot 10^{-3} \cdot \varepsilon + 9 \cdot 10^{-4} \cdot \varepsilon^2 - 2 \cdot 10^{-6} \cdot \varepsilon^3\right] \mathrm{MeV}, \tag{1.3}$$

where ε denotes the antineutrino energy in MeV.

Another consequence of the quasi-elastic scattering is the almost uniform angular distribution of the positron momenta, especially at neutrino energies between 10 and 20 MeV (see Fig. 1.2). For very low energies the mean cosine of the scattering angle is slightly negative, then it crosses zero at about 15 MeV. At higher energies the distribution becomes more and more forward-peaked [58].

Electron Scattering

Elastic scattering off electrons

$$\nu + e^- \rightarrow e^- + \nu \tag{1.4}$$

is possible for all neutrino flavours and hence the main reaction for all neutrino species except $\bar{\nu}_e$. Its cross-section can be calculated from the standard model prediction for the weak interaction [41]. It is significantly lower than the cross-section of inverse beta decay and proportional to E_ν instead of E_ν^2.

Reactions with Oxygen

As an oxygen nucleus is a compound object with a shell structure, it offers reactions to both $\bar{\nu}_e$ and ν_e, in the form of charged (CC) as well as neutral currents (NC).

The main contributions are:

$$^{16}O + \nu_e \rightarrow {}^{15}O + e^- + p \quad \text{(CC)} \tag{1.5}$$
$$^{16}O + \bar{\nu}_e \rightarrow {}^{15}N + e^+ + n \quad \text{(CC)} \tag{1.6}$$
$$^{16}O + \nu_e \rightarrow {}^{14}N^* + e^- + 2p \quad \text{(CC)} \tag{1.7}$$
$$^{16}O + \nu_e \rightarrow {}^{15}O^* + e^- + p + \gamma \quad \text{(CC)} \tag{1.8}$$
$$^{16}O + \bar{\nu}_e \rightarrow {}^{16}N + e^+ \quad \text{(CC)} \tag{1.9}$$
$$^{16}O + \bar{\nu}_e \rightarrow {}^{15}N^* + e^+ + n + \gamma \quad \text{(CC)} \tag{1.10}$$
$$^{16}O + \nu \rightarrow {}^{15}N + \nu' + p \quad \text{(NC)} \tag{1.11}$$
$$^{16}O + \nu \rightarrow {}^{15}N^* + \nu' + p + \gamma \quad \text{(NC)} \tag{1.12}$$

These reactions and their cross-sections are discussed in [34]. The NC reactions are not visible in a water Cherenkov detector as there are no energetic charged leptons in the final state. The CC reactions strongly depend on the neutrino energy as their cross-sections rise steeply once the (rather high) threshold of about 13 MeV and 18 MeV for the interactions with ν_e and $\bar{\nu}_e$, respectively, is reached (see fig. 1.3). Depending on the energy spectrum of the incident neutrinos (see section 1.2.2), at high energies these can account for a rather large contribution to the whole signal.

In [55], a fit of the ν_e charged current cross-section has been performed according to the parametrisation

$$\sigma(E_\nu) = A \cdot \left[(E_\nu/\mathrm{MeV})^B - C^{\frac{1}{4}} \right]^D , \tag{1.13}$$

which is also appropriate for the other cross-sections. The parameters are given by:

Reaction channel	A	B	C	D
ν_e charged current [55]	$4.7 \cdot 10^{-40}\,\mathrm{cm}^2$	$\frac{1}{4}$	15	6
$\bar{\nu}_e$ charged current	$3.1(6) \cdot 10^{-40}\,\mathrm{cm}^2$	0.223(3)	8.0(5)	5.9(3)
all ν neutral current	$6.7(8) \cdot 10^{-40}\,\mathrm{cm}^2$	0.208(8)	8.0(2)	6 (fixed)

Although the polar ice is very pure, meaning that there are only few inclusions of dust or air, of course its isotope ratio resembles the natural one. This means that there is a small amount of ^{18}O, ^{17}O, and deuterium. Their contribution to the signal in the SuperKamiokande detector due to solar ^{8}B neutrinos is discussed in [25]. From this and the accurately known ^{8}B neutrino spectrum [10], the cross-section can be inferred. As it is significantly lower than the ^{16}O cross-section and there are much fewer targets for this reaction (^{18}O as the most abundant of the three does only make up about 0.2 % of natural oxygen, for the abundances see [38]), those three isotopes are only relevant below the ^{16}O threshold. A rather large fraction of the

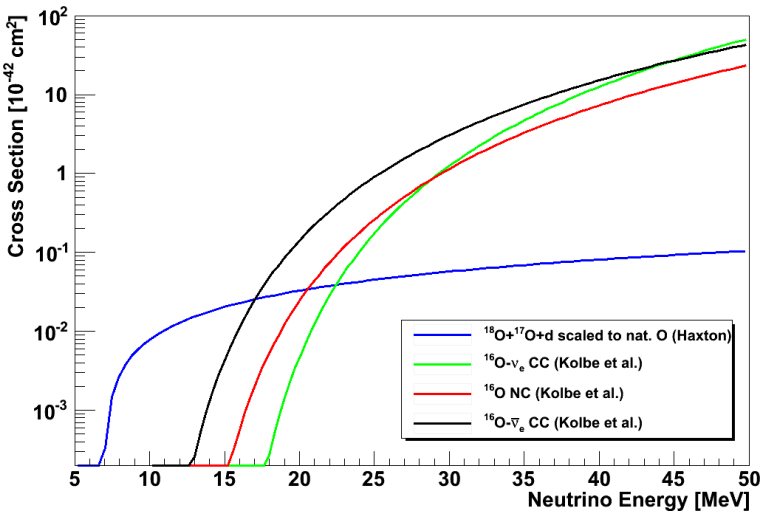

Figure 1.3: Neutrino cross-sections on natural oxygen according to Kolbe et al. [34] and Haxton et al. [25]. Note that the $^{18}\mathrm{O} + {}^{17}\mathrm{O} + d$ cross section is scaled to the abundance of ^{18}O in natural oxygen.

primary neutrino spectrum may cover this region though, so—again depending on the actual spectral shape—the contribution might need to be taken into account. A quadratic fit to this cross-section gives the following result:

$$\sigma(E) = \left[0.17(2)\left(\frac{E}{\mathrm{MeV}}\right)^2 + 1.6(5)\frac{E}{\mathrm{MeV}} - 0.9(2)\right] \cdot 10^{-45}\,\mathrm{cm}^2 \quad . \tag{1.14}$$

1.1.3 Detection of Neutrinos in Ice

The medium for the detection of neutrinos in the IceCube neutrino detector is the glacial ice at the geographical South Pole with which they can interact in different ways as described in the previous section. Common to most of these reactions is a charged lepton (positron or electron) in the final state, which carries most of the primary neutrino's energy, some ten or twenty MeV in the case of neutrinos generated in a supernova.

These energetic leptons are the key to the detection of neutrinos. The underlying physics will be discussed in the following section.

Energy Deposition of Charged Particles in Matter

The energy loss of charged particles in matter is mostly due to partial ionisation of the medium as the particles scatter off shell electrons. The theory of this energy deposition was developed in [13]. Later the screening of the electrical field and a linear term were added, that describes the bremsstrahlung resulting from interactions with the nuclei's electrical field at higher energies.

This leads to the so-called "Bethe-Bloch formula" [44]:

$$-\frac{\mathrm{d}E}{\mathrm{d}x} = \kappa_1 Z^2 \frac{n_e}{\beta^2} \ln\left[\frac{\kappa_2 \beta^2}{(1-\beta^2)I} - \beta^2 - \delta\right] + \kappa_3 E \quad . \tag{1.15}$$

Here the κ_i are material dependent constants, n_e is the electron density, I the mean ionisation potential, δ the screening of the electrical field, Z the particle's charge, and $\beta = v/c$.

As this relation is nearly constant in the MeV range, the mean track length of a particle before it is stopped (and annihilates in the case of a positron) should be proportional to its initial energy. This was confirmed in the `GEANT4` simulation which is the main part of this thesis (see Chapter 3) giving the relation (see Fig. 1.4)

$$\bar{x}_e(E) = 0.5662(1)\,\mathrm{cm} \cdot \frac{E}{\mathrm{MeV}} \quad . \tag{1.16}$$

In the simulation, only the track length was counted during which the particles were above the Cherenkov threshold (see Section 1.1.3), as the detection of particles with IceCube is carried out via the Cherenkov light they produce. Also, the term "track length" stands for the total track length and not the effective one, because the emission of Cherenkov light obviously occurs along the motion of a particle. The effective track length is the distance between creation and stopping of the particle and can be much shorter than the total due to multiple scattering.

The Cherenkov Effect

The energy loss of relativistic charged particles in matter is dominated by ionisation and bremsstrahlung as discussed above. In optical media those come along with the emission of photons in the optical and radio range called "Cherenkov effect". It occurs when a charged particle moves with a larger velocity than the local phase velocity of light,

$$v > c_{\mathrm{medium}} = c/n \quad . \tag{1.17}$$

For polar ice, the phase refractive index in the relevant region between 300 nm and 600 nm (vacuum) wavelength is $n_{\mathrm{ice}} \simeq 1.32$ [50]. So for electrons or positrons, the Cherenkov condition is fulfilled for kinetic energies above 272 keV.

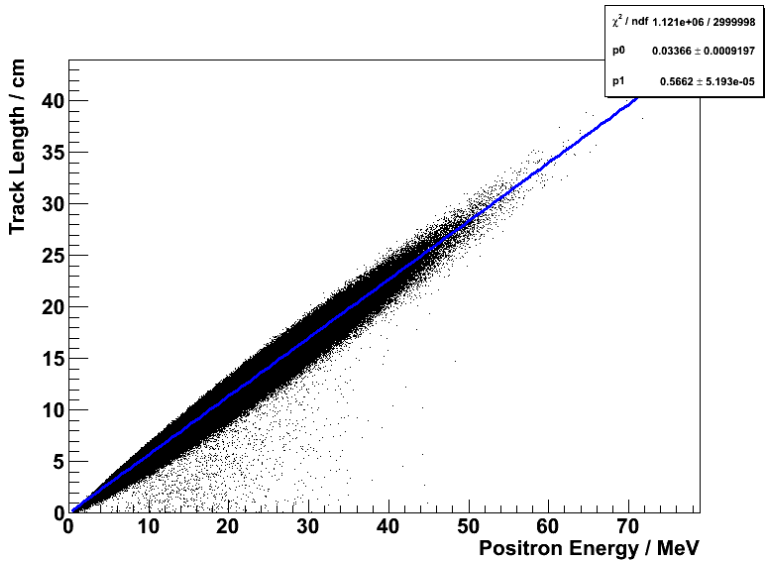

Figure 1.4: Mean track length of positrons in ice with line fit. `p1` is the gradient in cm/MeV.

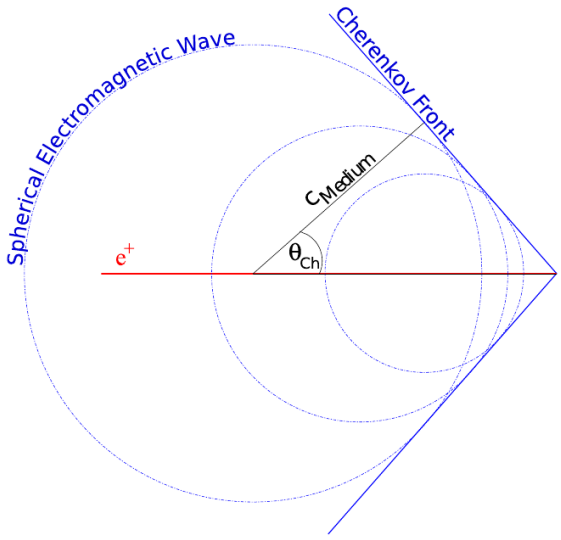

Figure 1.5: Illustration of the Cherenkov effect (schematic). Picture taken from [37]

Then the spherical electromagnetic waves emitted by the moving charge overlap in a way that they form a shock front of conical shape, called Cherenkov cone in analogy to the Mach cone that appears in supersonic motion (see fig. 1.5). Photons are emitted almost[1] rectangular to the shock front.

The opening angle of the Cherenkov cone is given by the relation

$$\cos\vartheta_{\mathrm{Ch}} = \frac{c_{\mathrm{medium}}}{v} = \frac{1}{\beta n} \quad . \tag{1.18}$$

It depends on the particle's velocity and hence its energy. As electrons and positrons of MeV energies are highly relativistic, $\beta \simeq 1$ is valid for most of their path within the ice so that

$$\vartheta_{\mathrm{Ch}} \simeq \arccos\frac{1}{n_{\mathrm{ice}}} \simeq 41^\circ \tag{1.19}$$

can be treated as constant.

The energy loss due to Cherenkov radiation is described by the Frank-Tamm formula, that can be found in [31]

$$\frac{\mathrm{d}E}{\mathrm{d}x} = \frac{(Ze)^2}{c^2}\int_{n(\omega)>1/\beta^2} \omega\left(1 - \frac{1}{(\beta n(\omega))^2}\right)\mathrm{d}\omega \quad . \tag{1.20}$$

This integral does not diverge as the refractive index drops below 1 in the ultraviolet region.

Its contribution to the total energy dissipation is, as mentioned before, marginal, but from this the rate of photon production can be inferred. Expressed as an energy spectrum, the number of photons generated per track length is [44]

$$\frac{\mathrm{d}^2N_\gamma}{\mathrm{d}x\mathrm{d}E} = \frac{\alpha Z^2}{\hbar c}\sin^2\vartheta_{\mathrm{Ch}} = \frac{\alpha Z^2}{\hbar c}\left(1 - \frac{1}{(\beta n(E))^2}\right) \quad , \tag{1.21}$$

where for simplicity the refractive index was treated as constant. Evaluating the constants, one finds for positrons (electrons) in polar ice:

$$\frac{\mathrm{d}^2N_\gamma}{\mathrm{d}x\mathrm{d}E} \approx 370\, Z^2 \sin^2\vartheta_{\mathrm{Ch}}\,\mathrm{eV}^{-1}\mathrm{cm}^{-1} \approx 175\,\mathrm{eV}^{-1}\mathrm{cm}^{-1} \quad . \tag{1.22}$$

One also often finds a version of this formula giving a wavelength spectrum [44]:

$$\frac{\mathrm{d}^2N_\gamma}{\mathrm{d}x\mathrm{d}\lambda} = \frac{2\pi\alpha Z^2}{\lambda^2}\left(1 - \frac{1}{(\beta n(\lambda))^2}\right) \quad . \tag{1.23}$$

Here the $1/\lambda^2$ dependency of the spectrum becomes evident[2]. When using this wavelength dependent equation, one has to bear in mind that λ always means the

[1] As group and phase velocity differ the angle is not quite 90°.

[2] This is the reason for the bright blue colour in which Cherenkov light appears to the human eye.

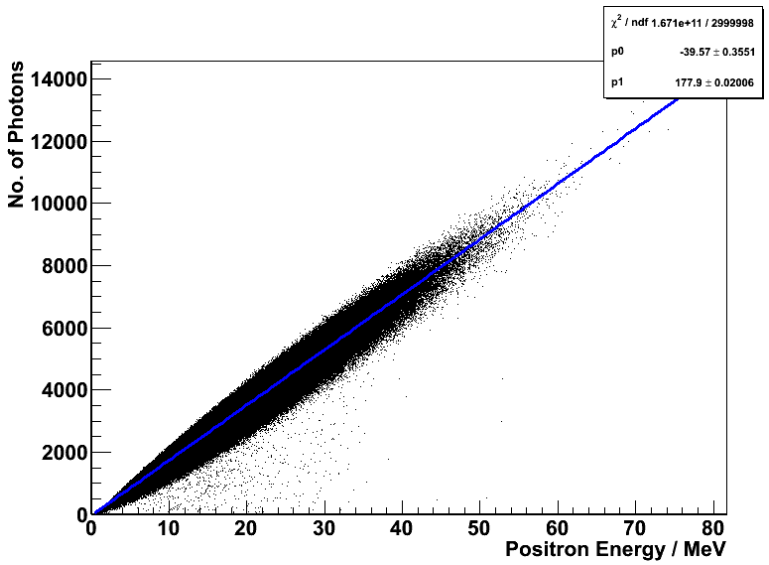

Figure 1.6: Cherenkov photon production by positrons in ice with line fit. The parameter `p1` is the slope in N_γ/MeV.

vacuum wavelength and not the wavelength in the medium that differs from that in the vacuum by a factor of n.

As mentioned above, the energy dependent expression can be treated as constant with good accuracy. Then the integration over a certain energy interval becomes trivial and one can easily estimate the number of Cherenkov photons for a certain particle. Again using the values for polar ice, the calculation yields a number of

$$\frac{\mathrm{d}N_\gamma}{\mathrm{d}x} = 325,8\,\mathrm{cm}^{-1} \tag{1.24}$$

photons in the visible range between 300 nm and 600 nm of vacuum wavelength.

This result can be combined with the mean path length that has been simulated (1.16) to estimate the number of Cherenkov photons produced by an electron or positron of given energy:

$$N_\gamma(E_e) = \frac{\mathrm{d}N_\gamma}{\mathrm{d}x} \cdot \bar{x}_e(E) = 183.95(3)\,\mathrm{MeV}^{-1}. \tag{1.25}$$

In the simulation, the number of Cherenkov photons was also counted directly, giving a smaller number of $N_{\gamma,\mathrm{sim}}(E_e) = 177.9\,\mathrm{MeV}^{-1}$ (see Fig. 1.6). The reason for this will be discussed in Section 4.1.

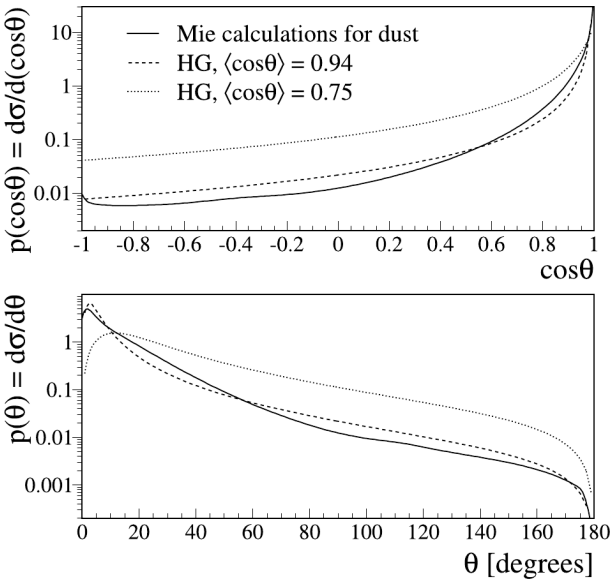

Figure 1.7: Scattering probability density function for dust particles in ice. Full Mie scattering calculation implies strongly forward-peaked scattering which can be approximated by a Henyey-Greenstein function (1.26) with $\langle \cos\theta \rangle = 0.94$ [6], while $\langle \cos\theta \rangle = 0.75$ describes scattering dominated by air bubbles [49]. Graph taken from [6].

Scattering of Light

In polar ice, the most important scattering centres are dust particles of micron size and microscopic air bubbles [6]. As those are on the same scale as the wavelength of Cherenkov photons, the simple Rayleigh scattering model is not applicable, which is only valid if the size of the scattering centres is negligable with respect to the photon wavelength.

So one has to consider the Mie scattering theory [43], which is a full analytic solution of the Maxwell equations in a regime where the scattering centres are represented by closed areas, for simplicity of spherical shape, that have a different refractive index from their surroundings. The numerical solutions of the Mie scattering integrals need a lot of computational effort to be carried out, hence a simple approximation is required for Monte Carlo simulations.

Such an approximation was found by Henyey and Greenstein when studying the propagation of radiation through the interstellar medium [26]. In their approximation, the scattering probability density function only depends on one parameter, the average cosine of the scattering angle for a single scatter, $\langle \cos\theta \rangle$. The closer this

parameter is to unity, the more forward-peaked is the scattering. For $\langle\cos\theta\rangle = 0$, the scattering is isotropic. Then the scattering probability density function reads

$$p(\cos\theta) = \frac{1 - \langle\cos\theta\rangle^2}{2\left(1 + \langle\cos\theta\rangle^2 - 2\langle\cos\theta\rangle\cos\theta\right)^{3/2}} \quad . \tag{1.26}$$

A comparison between the Henyey-Greenstein approximation and a full Mie calculation for a realistic mixture of dust particles is shown in Figure 1.7. As one can see, the correspondence between both is not perfect and the approximation tends to prefer large scattering angles, i. e. backscattering, but is sufficient for simulation[3]. Especially for supernova detection where no track reconstruction needs to be done, scattering is less important than absorption, as one needs to detect as many point-like neutrino events as possible.

1.2 Core-Collapse Supernovae

Core-collapse supernovae, also called type II supernovae, follow the final, explosive burning stages in the evolution of very massive stars that exceed about 8 solar masses ($M_\odot$). Especially during the last two decades, that saw a large increase of computer simulation capabilities, they have been an area of intense astrophysical studies.

Although a lot of progress has been achieved, the explosion mechanism is still far from being understood. One main problem is that the only observational information available are the optical light curves of supernovae that probe the surface of a supernova. However, as will be discussed below, the relevant processes occur close to the very core of an exploding star.

Thus, a high statistics observation of neutrinos generated in a core-collapse supernova would permit a wide range of tests of both different supernova models and neutrino properties.

1.2.1 Evolution of a Star

Birth of a Star

Stars form out of large clouds of interstellar gas, which mainly consists of primordial hydrogen and helium. These clouds can be the remnants of older stars that have already completed their life cycle and that have mostly dissolved in their constituents. In this case, the clouds also contain heavier elements that have been produced in the progenitors.

A gas cloud is held together by its own gravity, which counteracts the tendency to expand like an ideal unbound gas. If the cloud's temperature is low and its

[3] A better approximation can be found in [18].

density sufficiently high, gravity becomes dominant and the cloud collapses to form a new star. This is described by the Jeans criterion, which results from equating the gravitational with the thermodynamic kinetic energy of an ideal gas. A collapse occurs, when the mass of a gas cloud exceeds the Jeans mass given by

$$M_J = 3.7 \cdot \left(\frac{k_B T}{G\mu}\right)^{3/2} \cdot \rho^{-1/2} \quad . \tag{1.27}$$

Here, k_B is the Boltzmann and G the gravitational constant while T, ρ, and μ denote the cloud's temperature, density, and mean molecular weight, respectively [51].

During collapse, the gas cloud is condensed and heated. In the centre of the cloud this process takes place much more rapidly than in the outer regions so that the protostar is formed only from the innermost part. There, temperature and pressure increase up to a level at which eventually the fusion of hydrogen is ignited.

After ignition, the remainders of the initial gas cloud get blown away by the radiative pressure of the newly born star.

The Burning Stages

The era during the existence of a star which is usually called its "life" is marked by the fusion of light elements, especially hydrogen, to heavier elements. Although stars are very hot and energetic objects even at their surface, this happens only in the innermost core as only there temperature and pressure are high enough to ensure that the fusion process is sufficiently effective that it is actually releasing energy rather than consuming it.

The first and longest burning stage is the fusion of hydrogen to helium. Effectively, this is carried out via the reaction

$$4\,p \rightarrow {}^4_2\mathrm{He} + 2\,e^+ + 2\,\nu_e + 26.73\,\mathrm{MeV} \quad . \tag{1.28}$$

However, this reaction will not occur in one single step but rather requires intermediate stages or catalysts. Two different mechanisms are known that effectively provide the fusion reaction, the pp chain and the CNO cycle. As the names imply, the pp chain is a multiple step reaction chain while the CNO cycle is a catalytic reaction involving carbon, nitrogen, and oxygen. Which of both will be dominant is highly dependent of the central temperature and hence the mass of a given star as well as on the availability of the catalysts. In rather light stars like the sun with low central temperatures, energy production will be due to the pp chain.

The first step in the pp chain is the fusion of two protons to deuterium,

$$p + p \rightarrow d + e^+ + \nu_e \quad . \tag{1.29}$$

As this is a weak process similar to inverse beta decay between two protons that repel each other due to Coulomb force, it takes an average of $9 \cdot 10^9$ years to happen [51].

In fact, this very low rate of the first step is the limiting factor for the whole pp chain.

Once a deuteron has been produced, it fuses with another proton to give helium 3,

$$d + p \rightarrow {}^{3}_{2}\mathrm{He} + \gamma \ . \tag{1.30}$$

Up to this step, only 6.93 MeV of the total 26.73 MeV have been released, 0.42 MeV plus another 1.02 MeV from positron annihilation in the first and 5.49 MeV in the second step[4] [51].

From here, the production of the final helium 4 has three different ways to take place, whose relative probabilities again depend on the central temperature of the star. In the sun with its low temperature, the so-called "pp chain I" contributes about 86 % of the total energy release. Here two helium 3 nuclei are directly fused to helium 4,

$${}^{3}_{2}\mathrm{He} + {}^{3}_{2}\mathrm{He} \rightarrow {}^{4}_{2}\mathrm{He} + 2\,p \ . \tag{1.31}$$

At higher temperatures, the dominant reactions are the pp chains II and III which are catalysed by an already existing helium 4 nucleus and involve lithium and beryllium, respectively, as intermediate states. Although in the sun those reactions do not account much of the energy production, they are of some importance for the understanding of the fusion processes in the sun as they include the generation of neutrinos with MeV energies. These neutrinos can be detected on the earth and from their flux the rate of the different reactions within the sun can be inferred. This has been done since the 1960s, confirming the predicted solar neutrino fluxes with good accuracy when taking neutrino oscillations into account (see Section 1.1.1).

Given that the star has a sufficiently high abundance ($\gtrsim 1\,\%$) of heavier elements, at central temperatures over about 20 million Kelvin energy production will be carried out predominantly via the CNO cycle. In contrast to the pp chain, this is a carbon catalysed reaction involving nitrogen and oxygen leading to an enrichment of the latter. Additionally, there exist branching points from which a rather complex network of catalysed reactions develops, ultimately leading to the production of even heavier nuclei like fluorine, neon, sodium and others up to silicon. But due to their higher charge and hence higher Coulomb repulsion, the production of heavy elements is strongly suppressed and does only occur in a relevant amount in stars with very high central temperature, i. e. very massive ones [51].

Hydrogen burning via the pp chain or CNO cycle is the main phase in the life cycle of a star, covering over 90 % of its lifetime. Depending on its mass, hydrogen burning lasts for several million up to some ten billion years. Heavier stars do actually live shorter because their additional fuel is overcompensated by their higher central

[4] This and the small cross section of deuterium production are the reason that all efforts to use fusion as a energy source use deuterium or helium 3 as precursor rather than hydrogen.

temperature and hence higher reaction rates. The relation between lifetime τ and mass of a star can be derived easily from the empirical mass-luminosity relation

$$L \propto M^{3.5}. \tag{1.32}$$

where the exponent slightly depends on the star's composition, and assuming that the amount of nuclear fuel, i. e. hydrogen, available for a star is proportional to its mass. This leads to

$$\tau \propto M/L \propto M^{-2.5}. \tag{1.33}$$

Once the hydrogen in the core is exhausted, the burning zone has to move outwards in order to find enough fuel to sustain hydrogen fusion. In the very centre of the star, energy production via hydrogen burning is interrupted and so the gravitational force is no longer balanced by thermal pressure. Consequently, the core collapses and heats up due to the increasing density and pressure. At some point the central temperature rises sufficiently to ignite helium burning, which then releases enough energy to stabilise the now more compact core and inflate the outer parts to several times their original size. The surface will cool down due to its increased size, hence taking on a more reddish colour. Therefore, stars in this burning stage are called red giants.

The mechanism of helium burning and the production of heavy elements, especially carbon, is a rather unusual reaction called the triple-alpha process. Given the known cross sections of all conventional reactions between light nuclei, the observed abundance of carbon 12 in the universe cannot be explained and hence an other, more exotic reaction channel has to be available.

It turns out that there are nuclear resonances in both carbon 12 and the metastable beryllium 8 close to the mean energy of α particles in the stellar interior. These vastly increase the reaction cross section for the very unlikely event that three α particles collide almost simultaneously, first producing an unstable beryllium 8 nucleus which subsequently fuses with the third α to give carbon. The existence of these resonances was predicted from the observed carbon abundance years before actually observing them [15].

1.2.2 End of a Star

In its red giant stage, that typically lasts for some 10^8 years, the interior of a star consists of a core in which helium burning via the triple-alpha process takes place, stabilising the star. This is surrounded by a shell in which hydrogen burning and the production of heavier elements in the CNO and higher cycles as described above still occur.

At some point, also the helium fuel in the inner core will have exhausted, again leading to a rapid drop in thermal pressure and a further contraction of the core.

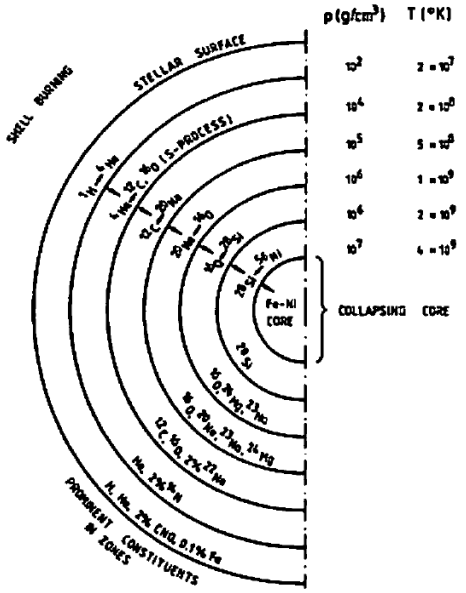

Figure 1.8: Inner structure of a pre-supernova giant star's core (schematic). Drawing taken from [51].

In rather light stars like the sun, no further burning stages can be reached and the collapsing stellar matter will be ultimately stabilised by the Fermi degeneration pressure of the free electrons. The result is a planet-sized compact object slowly cooling down by the emission of electromagnetic radiation, called a white dwarf.

In stars heavier than about $8\,M_\odot$ that have produced enough heavier elements, these can be used as additional fuel, allowing the star to enter further burning stages. This leads to a sequence of fusing the lightest elements available, using up all fuel in the core, further contraction and the ignition of the now lightest elements while the previous burning mechanism still occurs in a shell around the core. So the star develops an onion-like shell structure of regions with different burning stages (Fig. 1.8). As energy production gets more and more effective while the core is heated and compressed in higher burning stages and the amount of fuel is reduced with each stage, the duration of the single stages decreases from several thousand years for carbon down to seconds for silicon burning [51]. Also, the star becomes more and more prone to turbulences due to its high energy release and the complex shell structure, often leading to periodic changes in its luminosity or the ejection of its outermost parts.

Collapse

Ultimately, iron is produced in the very final burning stage. Being the most stable element (i. e. it has the highest binding energy per nucleon), the fusion of iron to heavier nuclei would consume energy rather than releasing it. No further energy production is possible at this point, thus the gravitational force has to be compensated by degeneration pressure of the free electrons rather than thermal pressure. The degeneration pressure can only be sustained while the mass of the iron core is below the Chandrasekhar limit of about $1.44\,M_\odot$ [17]. As iron is produced continuously during the final silicon burning, the core will eventually exceed the mass limit and start to collapse.

While the density of the collapsing core increases, free electrons will be captured by the nuclei, leading to the generation of both electron neutrinos and neutron-rich isotopes. Thereby the electron density is reduced, further accelerating the collapse. At some point, the central density reaches a value that is so high that the matter becomes opaque even for neutrinos. By then their escape time from the core exceeds the collapse time and they are essentially trapped inside the core (Fig. 1.9, upper panels).

The collapse continues until in the very centre the density and composition of nuclear matter is reached. Then this part is stabilised again by the degeneration pressure of the free protons and neutrons, which is much higher than that of the electrons. The outer parts of the core continue to infall, hit the "solid wall" of the inner part and are reflected, forming a shock front now moving outwards again (Fig. 1.9, middle left).

For nuclear matter, a mass limit similar to the Chandrasekhar limit exist, the Tolman-Oppenheimer-Volkoff limit of about $3\,M_\odot$ [54, 45]. If the collapsing core exceeds this mass, a black hole is formed directly and the supernova cannot explode.

Explosion

From this point, the mechanism that ultimately triggers the final explosion is an area of intensive research and not yet fully understood. As it cannot be observed directly, computer simulations have to be used for its study. These are highly dependent on the models of the stellar interior as well as the limits of the simulation, for example its dimensionality and the incorporation of relativistic kinematics. For an overview of different simulations and a detailed description of the explosion mechanism, see [32, 35].

Most simulations agree that the expanding shock front does not directly cause the explosion and is not even capable of stopping the collapse. Its energy is consumed rapidly by dissociating the infalling heavy nuclei into free neutrons and protons which have, relative to their progenitors, a largely enhanced cross section for electron

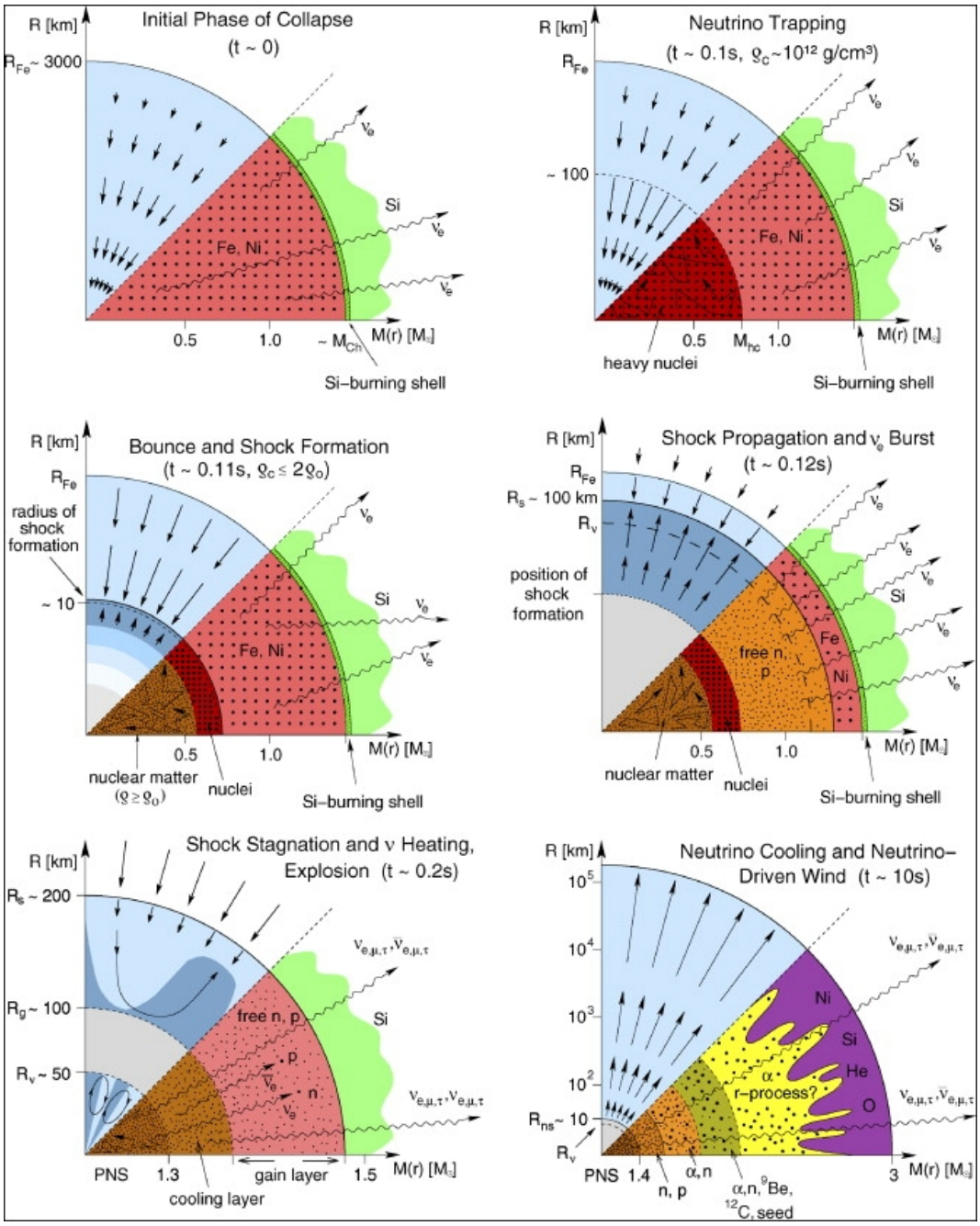

Figure 1.9: Mechanism of a core-collapse supernova (schematic). In the panels, the kinematics within the star is displayed in the upper halves, the arrows representing mean velocity vectors. The lower halves show the composition as well as the nuclear processes taking place in the respective region and time. Drawings taken from [32].

capture. This leads to a short but very luminous emission of electron neutrinos which can escape the star, called deleptonisation burst (Fig. 1.9, middle right). From the initial collapse up to this point, only a fraction of a second has elapsed.

After the shock has stalled and the downstream of matter towards the stellar centre continues, the compact proto-neutron star (PNS) that has formed behind the shock front accretes more and more mass. Simultaneously, it starts to cool down by neutrino pair production and emission as those are the only particles that can leave the PNS. Together with the formerly trapped neutrinos generated in the initial collapse, they will undergo inverse beta decay (1.1) or its counterpart for electron neutrinos,

$$\nu_e + n \rightarrow e^- + p \ , \tag{1.34}$$

with the free protons and neutrons in the outer region, respectively. When enough electrons and positrons have been produced, the neutrinos, that are still emitted by the cooling PNS, scatter elastically and thermalise with the stellar medium, thus depositing energy and reheating it. Although less than 1 % of the total neutrino energy can be transferred to the stellar medium in this way, this is enough to revive the shock and finally cause the explosion of the whole star, which is facilitated by the fact that the shock front becomes unstable against convection as it moves outwards (fig. 1.9, bottom panels).

Neutrino cooling continues for several seconds during which the shock front is supplied with enough energy to make its way through the whole star and cause the ejection of the outer parts (note that all processes described above do only involve the innermost iron core). In the course of this, further nuclear reactions occur, that include the production of heavy nuclei beyond iron [51]. Typically, it takes several hours until the shock front does eventually reach the surface of the star and its optical luminosity starts to increase. By then, the processes in the stellar interior have ended and the PNS will have reached its final state after it has cooled down completely.

Neutrino Signature

Supernovae are easily detectable with optical telescopes as they usually develop a brightness similar to their hosting galaxy. Thus a large number has been observed during the last decades, giving rise to an estimate of their rate of two to three per century per galaxy [40]. However, optical observation can only provide information about the surface of a supernova which shows the first increase in luminosity only hours after the supernova actually happened and cannot probe its interior. So the processes in the very centre of star, the collapse of the core and the subsequent shock formation and explosion are obscured.

Neutrinos with $\mathcal{O}(10\,\mathrm{MeV})$ energies are produced in large amounts and involved in the core collapse as described above. Due to their extremely low scattering and

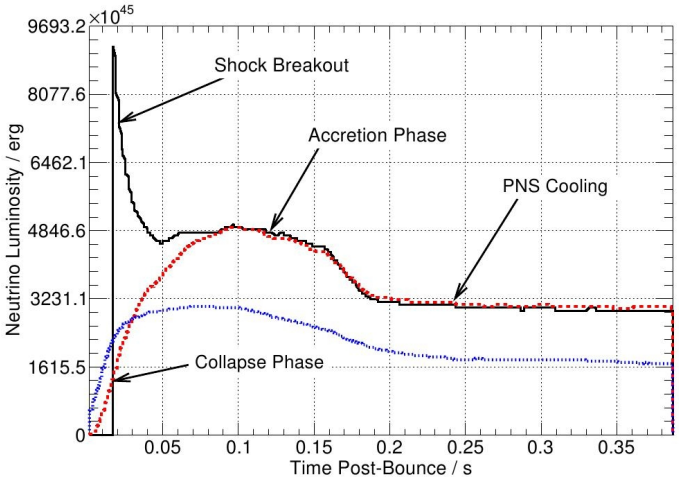

Figure 1.10: Neutrino luminosities of a one-dimensional supernova model with $15\,M_\odot$ progenitor mass [42]. Electron neutrinos are denoted in black, electron anti-neutrinos in red, and heavier neutrino flavours in blue. Graph taken from [37].

absorption cross sections, most of them can leave the supernova instantly and mostly undisturbed. Also, their mass is very low which means that they propagate essentially at the speed of light. So if the neutrino signal of a supernova is detected, there will be a lead time of several hours to record its optical light curve from the very beginning.

The energy spectrum of the neutrinos would be described as an ordinary Fermi-Dirac spectrum if they were produced in purely thermal processes,

$$f_{FD}(E,T,\mu) = \text{const.} \cdot \frac{E^2}{e^{(E-\mu)/T}+1} \quad . \tag{1.35}$$

For supernova neutrinos, the chemical potential μ is often set to zero while the neutrino temperature is approximately between 3 and 7 MeV.

However, it turns out that the neutrino spectrum is distorted due to various scattering processes off nuclear matter and leptons as well as pair production. This leads to a narrowed spectrum if compared to the corresponding, purely thermal one (1.35) which can be described by a modified version of the Fermi-Dirac spectrum that reads [33]

$$f(E,\langle E\rangle,\alpha) = \left(\frac{(\alpha+1)E}{\langle E\rangle}\right)^{\alpha+1} \cdot \frac{e^{-(\alpha+1)\cdot E/\langle E\rangle}}{E\cdot\Gamma(\alpha+1)} \quad . \tag{1.36}$$

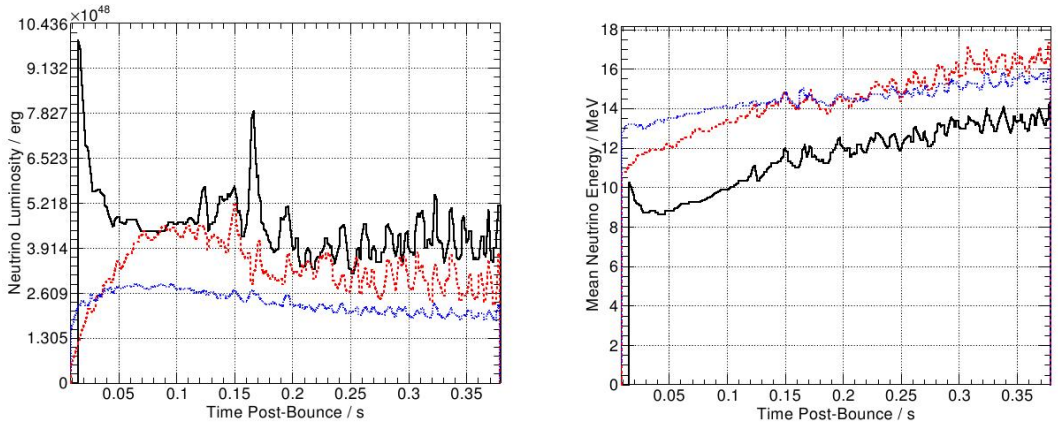

Figure 1.11: Neutrino luminosities and mean energies of a two-dimensional supernova model with 15 $M_\odot$ progenitor mass showing shock-instability induced modulations [42]. This particular model actually failed to explode. As above, Electron neutrinos are denoted in black, electron anti-neutrinos in red, and heavier neutrino flavours in blue. Graphs taken from [37].

Here, $\langle E \rangle$ denotes the mean neutrino energy which is usually between 12 and 30 MeV, and α is a parameter affecting the shape of the spectrum. Typical values of α lie between 2 and 5.

The neutrino signal itself, if recorded in sufficient detail, will provide information about the mechanism of the collapse that is not available in the optical light curve (see Fig. 1.10). Basically the following three features should be visible in which the recent simulations—at least qualitatively—agree [32].

At the very beginning there is the deleptonisation peak that results from the free protons generated by the initial shock front which then capture free electrons. This is the most luminous part of the whole neutrino light curve, which however, only lasts for a small fraction of a second. There is only a single reaction,

$$e^- + p \rightarrow \nu_e + n \quad , \tag{1.37}$$

that contributes to the deleptonisation peak which only produces ν_e. In water based neutrino experiments, reactions of ν_e are suppressed by a factor ~ 50 , making this channel very hard to detect.

The main part of the neutrino light curve is formed by the emission of neutrino pairs of all flavours during the cooling phase. The shape of this part is characterised by a sudden rise in luminosity followed by a decay over several seconds. Usually

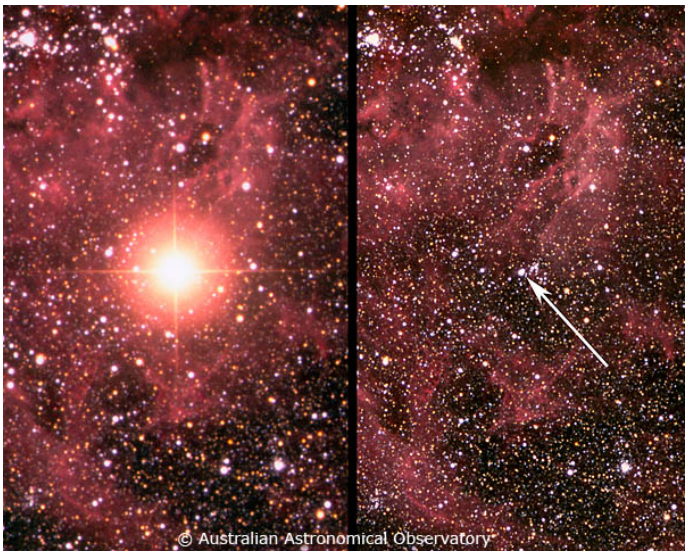

Figure 1.12: Sanduleak -69° 202a in the Large Magellanic Cloud pictured by the Anglo-Australian Telescope on February 5 (right) and March 10, 1987, before and after its explosion as SN1987A. Picture taken from [39].

the first phase, when the PNS is still accreting material, and the second, when it has reached its final size, are discernible. However, its exact form strongly depends on parameters like the stellar equation of state or the mass and composition of the progenitor star and varies in the different simulations. As additional effects, instabilities of the propagating shock front may cause a periodical modulation of the luminosity [42] and neutrino oscillation [35] can partially mix the spectra of the different neutrino flavours (see Fig. 1.11). The latter is relevant as the ν_e and $\bar{\nu}_e$ luminosities are significantly higher and their energies lower than those of the remaining flavours as they have more possibilities to interact with the stellar matter.

1.2.3 SN1987A

On February 24, 1987, the optical outburst of a type II supernova was observed in the Large Magellanic Cloud at a distance of about 50 kpc. It was the closest supernova recorded since Kepler's supernova in 1604 and the only one in the proximity of the Milky Way since the begin of modern astronomy. Hence it is also the most accurately observed and well-studied supernova up to now.

The progenitor was identified as Sanduleak -69° 202a [1], a blue supergiant with a mass of at least 11 $M_\odot$ probably in a binary system [47]. As it was the first supernova

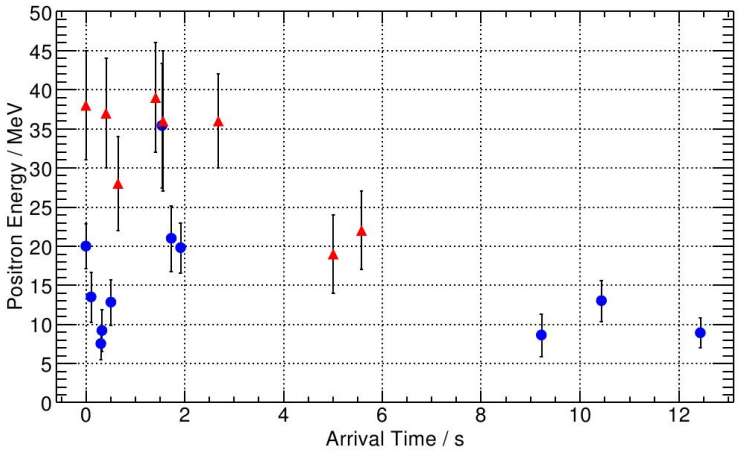

Figure 1.13: Neutrinos from SN1987A observed by Kamiokande-II (red) and IMB (blue). Due to timing uncertainties between the two experiments, the first event of each is used as time reference. The difference between the mean energies is caused by the different detection thresholds [35]. Graph taken from [37].

observed in 1987, it was named SN1987A.

Three of the neutrino experiments being operational at that time, the Kamiokande-II [27] and Irvine-Michigan-Brookhaven (IMB) [14] water Cherenkov detectors as well as the Baksan liquid scintillator experiment [8], saw a neutrino burst at approximately 7:35:40 UT on February 23, 1987, several hours prior to the first optical sighting. Nowadays, the Baksan events are not seen as being related to the supernova any more as the fiducial volume of the experiment was too small.

However, the $11 + 8$ supernova neutrinos detected by Kamiokande-II and IMB, respectively, were the first and up to now only neutrinos that could be related to a source outside the solar system. They proved that type II supernovae are actually related to the collapse of a massive star's core and the emission of a large number of neutrinos in the MeV range.

Although there were only 19 neutrinos detected, based on their energy and arrival times it was possible to infer the following limits on neutrino properties, e. g. their mass, charge, and lifetime [35]:

$$m_\nu < 13\,\mathrm{eV}, \qquad q_\nu < 10^{-18}\,e, \qquad \tau_\nu < 5 \cdot 10^{12} \left(\frac{m_\nu}{E_\nu}\right) \mathrm{s} \ . \tag{1.38}$$

2 Detector

In this chapter, the operation mode of water Cherenkov detectors for neutrinos will be discussed with special focus on the detection of supernovae. The setup and capabilities of the IceCube experiment and its components will be described in detail, as well as a possible low-energy extension, PINGU.

2.1 General

2.1.1 Water based Neutrino Telescopes

The term *neutrino telescope* refers to neutrino experiments which are aimed at the detection of neutrinos with extrasolar origin to study their overall flux and possibly discover point-like sources, which is commonly referred to as neutrino astronomy. In contrast, there are conventional experiments optimised for the study of artificially generated reactor or accelerator neutrinos, whose fluxes are high and well-known, so that their properties, especially oscillation parameters, can be analysed in detail.

Neutrinos open a whole new window to astronomical observation. Conventional optical telescopes can only probe the surfaces of astronomical objects while neutrinos, as in the case of a supernova that was described in the previous section, can act as direct messengers from the nuclear processes in which they are generated. Additionally, in the optical regime objects are often obscured by interstellar gas or dust clouds, or outshined by more luminous sources. Charged particles on the other hand do also carry information about nuclear processes and can be detected much more easily than neutrinos, but lose any directionality while passing through the earth's or interstellar magnetic fields.

For reconstructing their direction, the most promising candidates for neutrino astronomy are muon (anti-) neutrinos. In the detector, they will produce (anti-) muons that—given enough energy—live sufficiently long to produce a reconstructible track. Electron neutrinos will produce electrons that are subject to many interactions with matter, like electromagnetic cascades and bremsstrahlung, so that their tracks will be distorted, while tauons are too short-lived to leave an adequate track. However, even with muon neutrinos, neutrino astronomy usually aims at energies of more than 10 GeV as directional information can only be retrieved if there is a good correspondence between the directions of the incoming neutrino and the charged lepton that

is produced. The angle between both drops with energy. For $\nu_\mu \to \mu$ it is smaller than 1° only at about 10 TeV and beyond [30].

As neutrinos only interact with matter via weak a coupling, the detectors used in neutrino physics always consist of a large amount of active material that offers a reaction channel to neutrinos, and a detector that registers the reaction products. Often scintillators are used because of their good timing and reasonable energy resolution. In neutrino astronomy, however, fluxes are much lower and therefore larger fiducial volumes are needed. With a limited amount of financial resources, this can only be achieved with a more cost effective active material.

Water provides a large number of targets with a sufficient cross section for neutrino induced reactions and is widely available. Also, it is transparent and hence the detection of charged leptons via the Cherenkov photons they emit (see Section 1.1.3) is feasible. Depending on whether the focus of an experiment is more on lower energies and good resolution or on high energy events and high statistics, either artificial tanks filled with purest water, sometimes enriched with deuterium for an enhanced neutral current cross section or gadolinium for the detection of neutrons, or natural sites like the deep sea or polar ice are used as detectors. For the latter, a more opaque medium is accepted to maximise the detector volume.

Due to the very weak signal expectation, reduction of background from other cosmic or terrestrial radiation is crucial for all neutrino experiments, which is why most detectors are underground to use the above layers of rock, sea water, or ice, respectively, as shielding. For small experiments, the installation of a surrounding veto detector is an alternative.

2.1.2 Current Experiments

A number of water-based neutrino experiments is or has been operational during the last decades. Here, only those that are currently running and capable of supernova detection will be introduced.

Super-Kamiokande: Being the successor of the Kamiokande-II experiment that was involved in the detection of neutrinos from SN1987A (see Section 1.2.3), Super-Kamiokande was completed in 1996 and is operational since then. It is situated in the former Kamioka zinc mine in Japan, where an additional excavation now hosts the tank filled with 50 kton of purified water. The walls of the tank are covered with over 11000 photomultiplier tubes (PMTs) leading to an effective photocathode coverage of 40 % of the surface [22].

Therefore Super-Kamiokande offers a good energy and spatial resolution with extremely low background for MeV neutrinos which are the main topic of its research, namely solar neutrinos and proton decay signatures. Supernova neutrinos, as described above (Sec. 1.2.2), also have MeV energies and thus are easily detectable by

Super-Kamiokande. Due to its rather small volume, the total number of detected neutrinos, however, will be lower than e. g. in IceCube. On the other hand, this is compensated by the fact that Super-Kamiokande allows for a track, energy, and partial flavour reconstruction at these energies.

IceCube With over $1\,\mathrm{km}^3$ of glacial ice, whose instrumentation with 5160 PMTs was completed in December 2010, IceCube is the largest neutrino detector. Due to the high statistics that can be expected it shows the best sensitivity for galactic supernovae up to some 10 kpc distance. The experiment will be discussed in detail in section 2.2, 2.3, and 2.4.

ANTARES and KM3NeT In May 2008, the first neutrino telescope in the deep sea, ANTARES, was completed. It consist of a total of 900 PMTs on 12 strings that are installed between 2000 m and 2400 m depth in the Mediterranean sea near the French coast. Primarily it is meant as a proof of concept for the installation of a neutrino telescope in the deep sea and aims towards the construction of a similar experiment of km^3 size called KM3NeT which is scheduled for 2012. KM3NeT will then be the counterpart of IceCube on the northern hemisphere so that the observability of the whole sky is guaranteed [12].

As IceCube and KM3NeT are quite alike in design and size, their scope is also comparable and hence KM3NeT will be able to detect galactic supernovae while ANTARES has limitations in this due to its smaller volume. However, the drawback to the installation of a neutrino telescope in the deep sea is the strong background resulting from bioluminescence and $^{40}\mathrm{K}$ decay in the sea water [9] while glacial ice is a much purer environment.

2.2 IceCube

After its smaller predecessor AMANDA was successfully installed and commissioned as a proof of concept for a neutrino Cherenkov telescope in the deep ice at the geographical South Pole, the construction of IceCube began in 2005 and was finished on December 18, 2010. It aims at the detection of galactic neutrinos with highest energies from the northern sky, so the whole earth can be used as shielding against backgrounds, predominantly atmospheric muons.

2.2.1 Configuration

The IceCube detector consist of a total of 86 strings deployed into the polar ice, which has a thickness of about 2800 m at the pole, in an hexagonal pattern with 125 m inter-string spacing. For the deployment, a hot water drill is used to produce

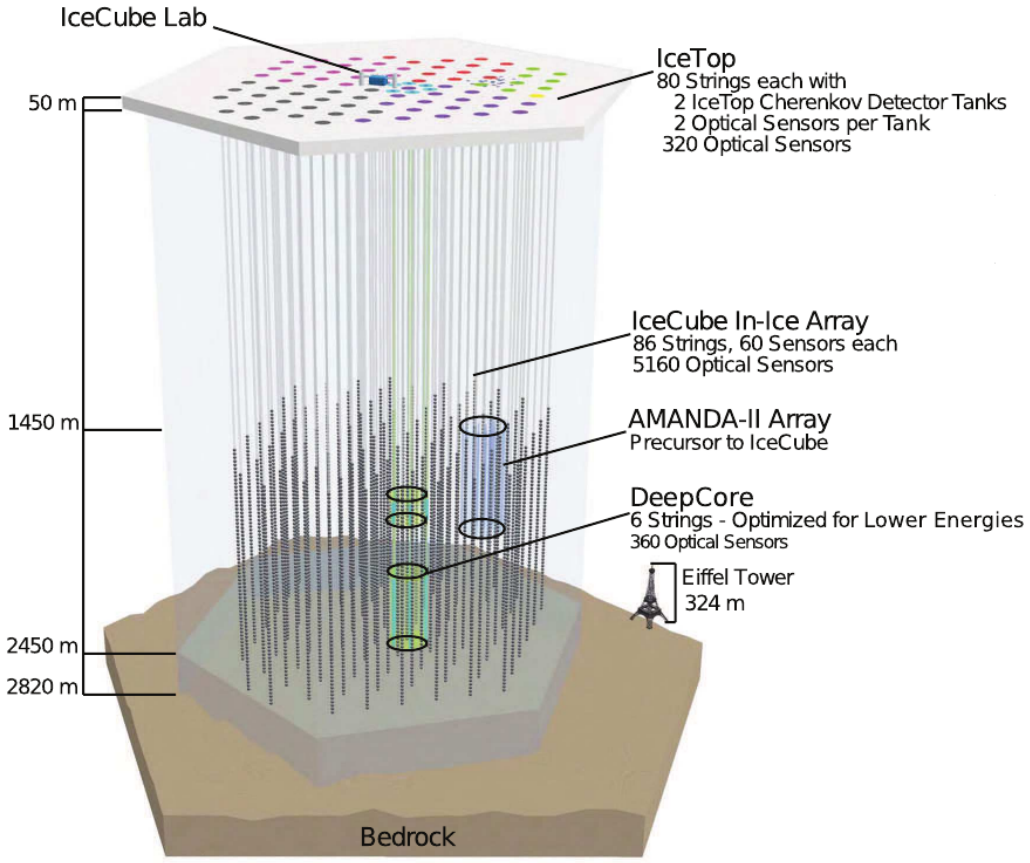

Figure 2.1: Schematic view of the IceCube neutrino detector along with its sub-detectors, taken from [2].

vertical holes with a diameter of 60 cm that reach to a depth of 2450 m. Then the strings are lowered into the holes still filled with water which then refreezes and firmly encloses the strings.

Between a depth of 1450 m and their lower end at 2450 m, 60 digital optical modules (DOMs) equipped with PMTs are attached to the strings, resulting in a vertical DOM spacing of 17 m, such that the total detector volume is roughly 1 km^3. This scale sets a lower limit to the track lengths that can be reconstructed, which corresponds to an energy of about 100 GeV [7].

To lower this threshold, six of the strings were positioned with a smaller spacing of only 72 m to form the DeepCore sub-detector. On the DeepCore strings, the DOMs are attached in two bunches above and below a dust layer that was found between 1950 m and 2100 m depth, with a DOM spacing of 10 m and 7 m above and below the dust layer, respectively. This lowers the energy threshold by one order of magnitude [59].

Additionally, on the surface of the ice shield IceTop was built, an array of ice filled tanks matching the IceCube string layout, so that two tanks were installed in the proximity of each IceCube string. Each of the tanks contains two IceCube DOMs to detect the Cherenkov light produced by air showers. Due to the high noise rates and missing shielding against cosmic rays, IceTop cannot be used for supernova detection.

The complete layout of IceCube including all sub-detectors is shown in Figure 2.1.

2.2.2 Ice Properties

The optical properties of the south polar ice have been studied in detail by the IceCube experiment as their comprehension is crucial for the reconstruction of particle tracks via Cherenkov light [6].

For the detection of supernovae, scattering is less important than absorption because one assumes a homogeneous illumination of the detector with tracks too short to be reconstructed (in the order of some tens of centimeters, see Section 1.1.3). So the absorptivity, which limits the total number of photons that can be seen by the detector, should be as small as possible. In fact, the very low scattering and absorption coefficient of polar ice that are of the order of several tens of meters are one of the main reasons for IceCube to be located at the South Pole.

As one can see from Fig. 2.2, the ice gets clearer at depths below 2100 m. This effect is more dramatic for scattering since close to the top it is dominated by small air bubbles that remain when newly fallen snow is compressed to ice. Deeper in the ice, these bubbles have been dissolved into hydrates by the pressure of the ice on top.

A prominent dust layer can clearly be seen roughly between 1950 m and 2100 m depth. Therefore, the proposed PINGU extension, which will be the main topic of

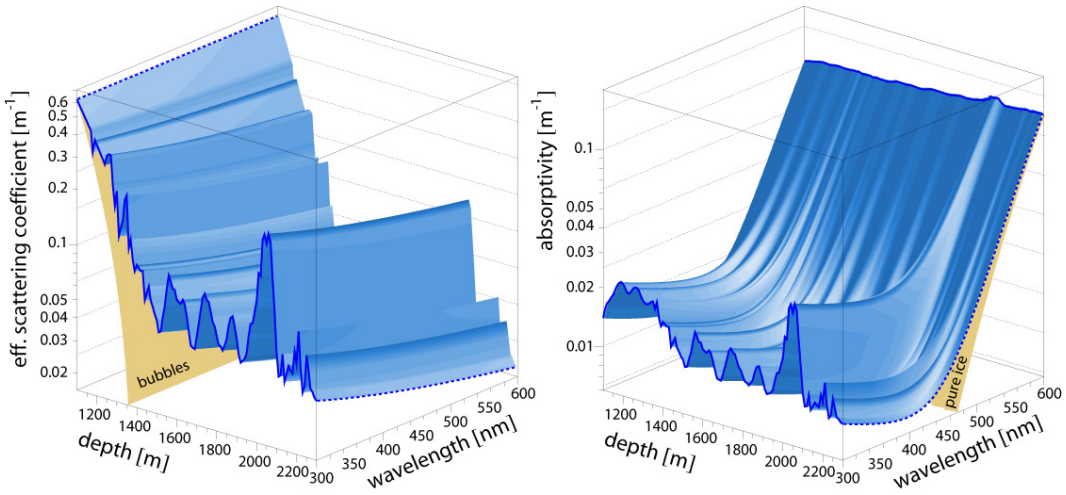

Figure 2.2: Effective scattering and absorption of light in the polar ice. Picture taken from [6].

this thesis, as well as the major part of the existing DeepCore extension to IceCube are situated in the very clear ice below the dust layer.

Another important feature of the ice instrumented by IceCube is the so-called "hole ice" which develops in the drill holes during refreezing and hence directly surrounds the optical modules. Early analyses of the hole ice in AMANDA found that the effective scattering length of hole ice is only 50 cm [48], which is significantly lower than in the bulk ice and effectively reduces the directionality of the DOMs. This value will be used for further calculation and simulation along with an estimated absorption length of 100 m. However, recent measurements imply an inhomogeneous structure of the hole ice with a very opaque inner part and a much clearer exterior [29].

2.2.3 PINGU

A possible further extension of IceCube that might be realised during the next decade is PINGU, which stands for Phased IceCube Next Generation Upgrade. Its final goal is the construction of a next-generation neutrino detector in the deep ice with a very low threshold in the MeV range and several megatons of fiducial volume, which is referred to as PINGU phase 2. Phase 1 is meant to be a smaller predecessor consisting of about 18 strings[1] centred around an existing IceCube or

[1]This number was chosen because it turned out during the construction of IceCube that up to about 20 strings could be deployed with one drill during one drilling season.

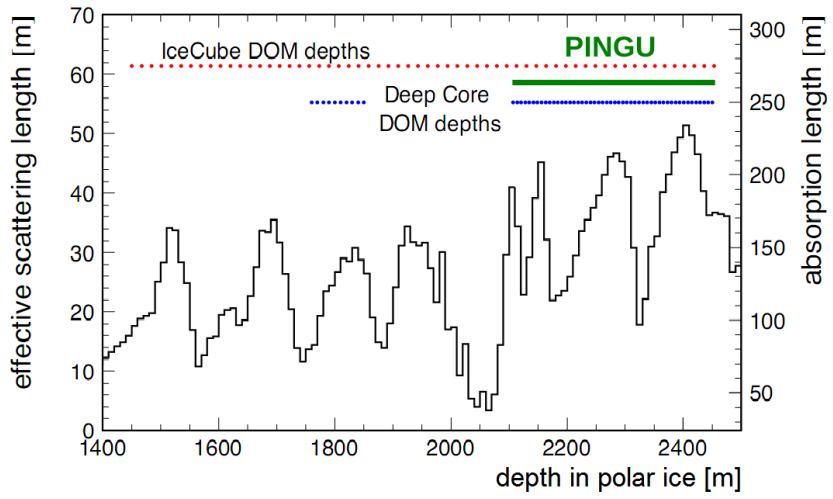

Figure 2.3: Position of PINGU in the deep ice compared with the current IceCube and DeepCore DOM positions.

DeepCore string with the DOMs attached in the depth of the lower DeepCore part, see figures 2.3 and 2.4. To reach very low energies, the string and DOM spacings in PINGU will be much smaller than in IceCube, between a few and some ten metres. This setup can also can be used for developing and testing new technology. Such a phased course of action has proved its worth in the AMANDA/IceCube experiments as well as in ANTARES/KM3NeT.

The physics goals of PINGU are those connected with the detection of MeV neutrinos. The study of supernovae in the Milky Way and its companions will already be possible in much more detail in phase 1 than in current experiments, which will be showed in this thesis. In phase 2 with its greatly enhanced fiducial volume, the reach might be extended to several Mpc so that also the neighbouring galaxies become visible. This would increase the rate of detectable supernovae from one each 30 to 50 years to a few per year. Although the reconstruction of their light curves will be challenging as the expected number of neutrino events from an extragalactic supernova is only some dozens, PINGU phase 2 could serve as an alert and possibly pointing device for optical telescopes.

Further goals are the search for proton decay in the polar ice which will be carried out with a larger fiducial volume than all previous experiments, indirect search for dark matter, and the detailed study of neutrino oscillation parameters with atmospheric neutrinos and possibly a future neutrino beam pointing towards the South Pole.

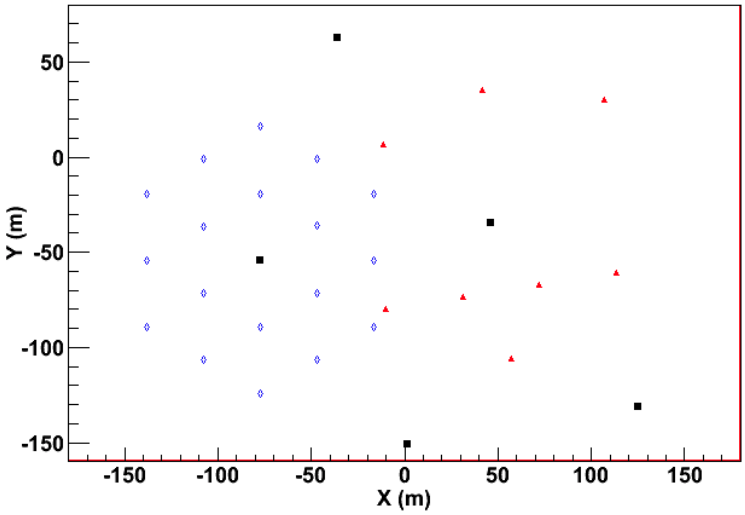

Figure 2.4: Possible geometry of PINGU phase 1. Existing IceCube and DeepCore strings are depicted in black and red, respectively. The proposed positions of the PINGU strings, here with a string spacing of 35 m, are marked in blue. Drawing taken from [21].

2.3 Digital Optical Modules

The 5160 Digital Optical Modules are the basic detection units of IceCube. They are attached to the string and connected to the main string cable during deployment and work autonomously except for the low voltage power supply. This modular design has the convenience that if one DOM fails to work and cannot be fixed as it is frozen in the deep ice, the others are not affected.

2.3.1 Design

As shown in Figure 2.5, the DOM is housed by a borosilicate glass sphere of 13" diameter and 0.5" thickness to withstand the pressure arising from the refreezing water in the drill holes. This glass sphere also contributes to the noise rate of about 540 Hz per DOM as it contains isotopes of the uranium and thorium decay chains. The content of natural ^{40}K, that undergoes beta decay where the emitted β particle generates Cherenkov light, has been reduced in the glass.

The main component of the DOM is a 10" PMT (Hamamatsu R7081-02 [4, 19]). It is oriented downwards as the main focus of IceCube is on galactic neutrinos from the northern hemisphere that have travelled through the Earth and hence arrive at the

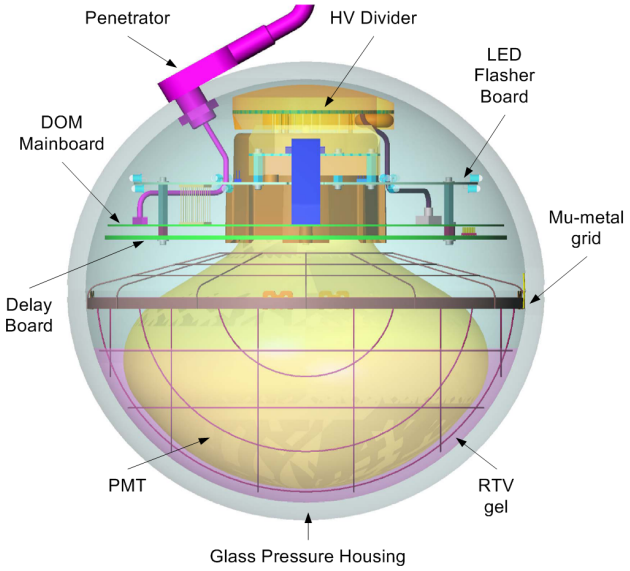

Figure 2.5: Schematic of an IceCube DOM, taken from [2]. For a detailed description, refer to the text.

South Pole from below. The coupling to the glass sphere is provided by an optical gel which also provides protection and fixation to the PMT, while a surrounding Mu-metal grid guarantees the shielding of external magnetic fields.

The upper half of the DOM is filled with an high voltage divider that locally transforms the 96 V voltage that is provided by the string main cable into the high voltage of 1.3 – 1.5 kV that is needed to fuse the PMT, thus making it independent from possible voltage fluctuations of the pole station's power supply. Around the HV divider, the circular flasher board and DOM mainboard are mounted. The flasher board is populated with LEDs that can be used to produce a standardised signal for calibration. On the mainboard the electronics are located that are needed to read out the PMT signal and digitise the recorded data in situ. So the raw PMT output does not need to be sent to the surface like in AMANDA, where it was subject to interfering effects along the 2 km cable path.

For a more detailed description of the DOM design refer to [7].

2.3.2 Quantum Efficiency and Angular Acceptance

The PMTs used in IceCube have been designed for a low noise level and a maximal sensitivity in the optical regime where the ice is transparent, peaking at a wavelength of 420 nm with a specified quantum efficiency of 25 % at 390 nm [19]. After

assembling a complete test DOM, its effective quantum efficiency has been studied in detail to establish the overall performance that could be expected from the DOMs that were deployed.

This was carried out by illuminating the fully assembled DOM with a light beam of 13" diameter and measuring the spectral response as well as the angular dependence of the signal relative to head-on lighting. The spectral response was tabulated. For the angular acceptance the following six parameter fit was found:

$$\begin{aligned} A &= 1.0 - 3.59 \cdot 10^{-3} x + 5.11 \cdot 10^{-5} x^2 - 4.27 \cdot 10^{-6} x^3 \\ &\quad + 5.56 \cdot 10^{-8} x^4 - 2.73 \cdot 10^{-10} x^5 + 4.76 \cdot 10^{-13} x^6 \ , \end{aligned} \tag{2.1}$$

where x denotes the zenith angle in degrees [60].

As one can see from Figure 2.6, the peak value of the quantum efficiency is only about 14 % rather than the specified 25 %. The reason for this is that the quantum efficiency was averaged over the whole DOM area that is visible head-on, including the outer part around the DOM, where the quantum efficiency is zero. The angular acceptance (Fig. 2.7) decreases towards large zenith angles like one would expect. The fact that it slightly increases again when approaching 180° is an artefact of the performed fit.

The angular dependence of the DOM acceptance, as mentioned above, is given relative to its peak value so that multiplying both for a given wavelength and zenith angle of an incoming photon provides the probability for the photon to be registered by the DOM. This probability is not quite exact since the values are always averaged over the visible DOM surface, but if the number of photons is sufficiently high taking the averages is justified.

In DeepCore an advanced version of the Hamamatsu R7081-02 PMT with a different photocathode material was used whose quantum efficiency is increased by about 35 %. At the same time the noise rate rises to $\sim$ 720 Hz [59]. Since the noise is not purely Poissonian but shows a burst-like behaviour, it can be reduced to about 50 % by applying an artificial dead time [24]. These high quantum efficiency DOMs would also be used in PINGU phase 1, probably along with other concept light sensors that need to be tested for their possible use in phase 2.

2.4 Supernova Detection

The main purpose of IceCube is the detection of high energy muon neutrinos and muons with track a length of typically several hundreds of metres, corresponding to the scale of the IceCube structures. This job is done by the main IceCube data acquisition software called pDAQ along with further trigger and reconstruction modules that basically search for coincident signals from different DOMs and then try

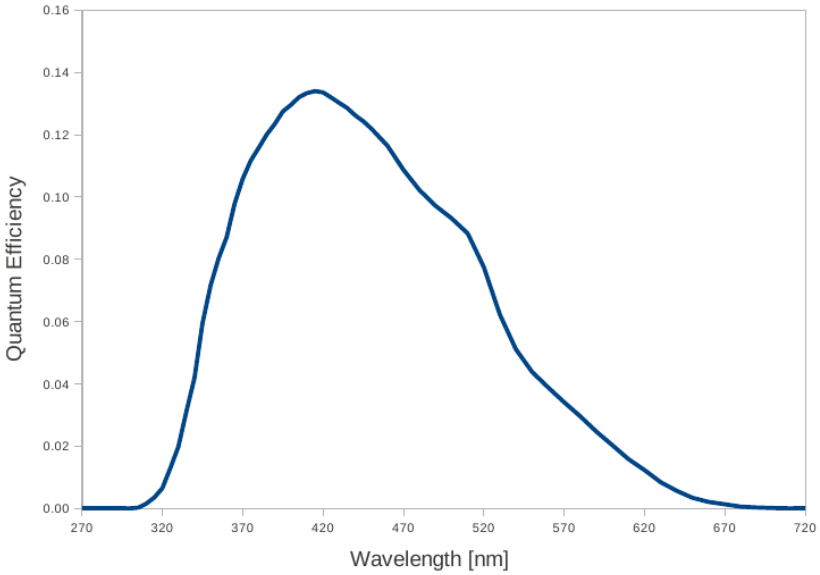

Figure 2.6: Effective quantum efficiency of a fully assembled IceCube standard DOM. Values taken from [60].

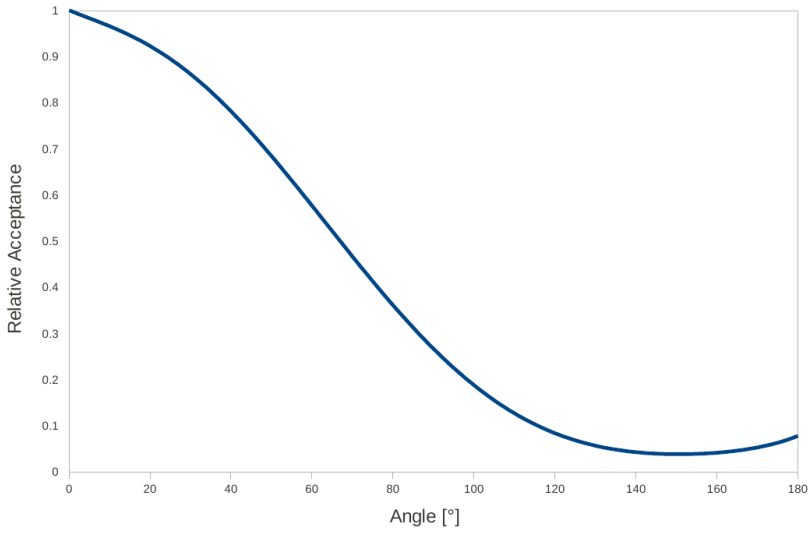

Figure 2.7: Relative angular acceptance of an IceCube standard DOM (2.1). Values taken from [60].

to find the straight line that best fits the time and position information the DOMs provide.

Supernova neutrinos on the other hand have energies in the 10 MeV range and generate positron tracks of a few cm length as described above (Sec. 1.1.3). For the typical DOM spacings in IceCube they look like a point-like source of Cherenkov light that only hits a single DOM so that no track reconstruction is possible. Thus the signature of a supernova in IceCube is in fact a collective and very homogeneous increase in the noise rates of all DOMs that follows the course of the neutrino light curve in time.

The continuous monitoring of the noise of all DOMs is a job that is contrary to what the pDAQ is designed for and hence supernova detection needs to be run parallel and mostly independent from the main IceCube operation. Therefore an additional 8 bit counter purely dedicated to supernova search was installed on each DOM's main board, recording all noise events that otherwise would have been discarded by triggers. The counters are internally binned in 1.634 ms intervals after which the count rates are sent from the DOMs to the supernova data acquisition (SNDAQ) software. The SNDAQ collects the asynchronously arriving data from the DOMs, rebins them to 2 ms and 500 ms intervals and calculates a significance for the whole detector [37].

The significance $\mathcal{S}$ is given by the ratio of the mean collective rate deviation and its variance,

$$\mathcal{S} = \Delta\mu/\sigma_{\Delta\mu} \quad . \tag{2.2}$$

From a likelihood approach, they were calculated to be

$$\Delta\mu = \sigma^2_{\Delta\mu} \cdot \sum_{i=1}^{N_{\mathrm{DOM}}} \frac{\varepsilon_i(r_i - \mu_i)}{\sigma_i^2} \tag{2.3}$$

and

$$\sigma_{\Delta\mu} = \left(\sum_{i=1}^{N_{\mathrm{DOM}}} \frac{\varepsilon_i^2}{\sigma_i^2} \right)^{-1/2} \quad , \tag{2.4}$$

respectively. Here, N_{DOM} is the total number of DOMs and r_i, μ_i, and σ_i are the current rate, mean and variance of each individual DOM. While r_i is directly taken from the data in 500 ms bins, μ_i and σ_i are calculated from the DOM's rate within five minutes each before and after the analysis window of 60 s that currently scanned for a supernova signature. ε_i finally is an individual weight that takes the slight differences in the quantum efficiencies of the DOMs into account. A more detailed description of the SNDAQ and how the analysis algorithm is implemented can be found in [46].

For PINGU, this approach would also be applicable. However, a conceptual gain would be advantageous. Especially when searching for extragalactic supernovae, the

crucial point is the reduction of background. As the DOM spacings will be much smaller, the probability for a single MeV positron produced by a supernova neutrino to be seen in more than one DOM is due to rise. So changing from counting the total noise rates towards an event-based approach in order to reduce background by counting "real" supernova events might become feasible.

Whether a cleaner signal can be obtained in this way will be discussed in the following.

3 Simulation

The main topic of this thesis was to create a detector simulation for study of the performance of the proposed PINGU phase 1 detector in terms of its capabilities to detect core-collapse supernovae. This simulation was written within the C++ based `Geant4` framework, a simulation software for particle and nuclear physics. Although `Geant4` was originally designed for high energy physics, it has extensions for lower energies. For this work it is important that also the behaviour of optical photons has been implemented [3].

The properties of this simulation, called `I3_Sim`, will be described in this chapter. Its source code is available at `http://code.icecube.wisc.edu/projects/icecube/browser/sandbox/lschulte/I3_Sim`.

3.1 Geant4

`Geant4` is a modularly designed software package for the simulation of high energy and nuclear physics experiments. It provides readily implemented routines for all well-established physics processes so that they can be easily integrated in any simulation.

A typical `Geant4` simulation's main function only contains the instantiation of the most important objects which will be described below. Additionally, some global options can be set.

The most vital objects of a `Geant4` simulation are:

RunManager: The run manager is the core of each simulation. All other objects in the main function have to be passed to it so that it is able to control the correct procedure of the whole simulation. Hence it does not need to be modified in a particular simulation. In fact the run manager is designed to handle all possible configurations a `Geant4` based program can have.

The run manager keeps control over the simulation throughout the complete hierarchy of the simulation process that is organised as follows:

The run represents the top level of the simulation process. A single run is the smallest amount of processing that can be initialised "by hand". During its execution, the properties of the simulation, i. e. the detector geometry, involved physics processes, and the like, cannot be changed.

The event is the next lower level. A run consists of one or more events. An event corresponds to the highest level physics event. In a collider simulation, for example, an event is one single collision while a run is a collection of several events.

The track corresponds to a single particle that is involved in an event. It reaches from the point where the particle is generated to where it decays or stops. During the track, secondary particles can be produced, for which new tracks are then created.

The step denotes the lowest level of simulation, each track being made up of many steps. For each step of each particle, its interaction lengths for all physics processes it is involved in are calculated and the step length is adjusted accordingly.

The following classes are each implemented in `Geant4` as abstract base classes which have to be filled by the user in a way that the run manager can handle the provided information.

PhysicsList: As the name suggests, the physics list has to contain all relevant particles and processes that should be included in the simulation. For the user this means that the corresponding objects have to be instantiated and the processes need to be assigned to the particular particles. As an option, energetic cuts can be set manually for particular processes to achieve a better computing performance when only a certain limiting case is of interest in the simulation.

DetectorConstruction: In the detector construction class, the geometry of the detector, that is to be simulated, is specified. The components of the detector have to be constructed in an hierarchical manner, meaning that each object is defined relative to the object containing it. This has the advantage that if an object is moved or copied, all its substructures are moved or copied, too.

The definition of a single object occurs in three steps. First, the pure geometrical shape of the object has to be specified. Many different shapes like boxes, spheres, tubes etc., that in addition can be combined in many ways, are provided. In the second step, a material is assigned to the shape, making it a logical volume. Finally, a physical volume is achieved, when a mother logical volume and a placement relative to the mother volume is specified. So the logical volumes contain all hierarchical information of the geometry. Therefore it is easily possible to produce identical copies of a certain detector part with its complete substructure simply by placing it more than one time. In addition, it is also possible for repeatedly placed volumes to modify some of the copies' properties as a function of the copy number.

Apart from the geometrical layout of the detector, also the materials they consist of need to be defined in the detector construction class. Chemical elements are provided and can also be created by specifying their charge number and molecular weight. From these, materials can be defined as a mixture of different elements or different materials with certain mass fractions and a mean density. If one is interested in optical processes, the optical properties of a material also need to be assigned at this point.

SensitiveDetector: Each part of the detector geometry that is supposed to act as an active part needs a sensitive detector object assigned to it. In this class it has to be specified how the active detector should react to an incoming particle, i. e. if a certain particle is registered at all and if yes, which physical quantities are stored in which manner.

PrimaryGeneratorAction: This class is responsible for the generation of primary particles for each generated event. This can be single particles as well as e. g. a complete air shower. All the primary's properties like identity, energy, position, direction, and others are fully controllable.

Other UserAction Classes: For each level in the simulation—run, event, track, and step—there is a corresponding user action class that provides handles to access the current stage of simulation and perform certain tasks the user has specified. This is useful for analysing events, as this is the place where the information that should be recorded and written to a file is collected and put in the respective containers.

3.2 I3_Sim

The configuration of the `I3_Sim` simulation will now be described in detail, following the sequence of classes described in 3.1.

3.2.1 Setting the Simulation Properties

`I3_Sim` is designed to be very flexible in its properties to enable the detailed testing of possible configurations as well as varying neutrino spectra or ice models without the need of changing its source code and recompiling it. Thus the configuration can be specified in a configuration file, a simple text file that is passed to `I3_Sim` as a parameter. The configuration file commands, that will be accepted by the simulation, are listed in the table overleaf.

Key	Parameter Format	Default	Effect
ResultsFile	<filename>.root	histograms.root	Changes the name of the file in which the output is stored.
IceTableFile	<filename>	Ice_table.aha. i3coords.cos080. 17may2007.txt	Changes the ice model, be careful that the formatting in the new file is exactly equal to the default one.
NumberOfEvents	<int>	none	Forces the program to process the specified number of events in batch mode.
DetectorLower Boundary	<double> *<length>	-505*m	Sets the lower end of the detector in IceCube coordinates.
DetectorHeight	<double> *<length>	350*m	Sets the height of the detector.
StringSpacing	<double> *<length>	5*m	Sets the inter-string spacing.
NoDOMsPer10m	<int>	10	Sets the number of DOMs on a single string per 10 m ice layer.
OverallEfficiency Factor	<double>	1	Gives the ability to tune the overall efficiency of the DOMs.
UsePerfectDOM	<bool> (i.e. 0 or 1)	0	DOMs produce a hit for each photon, i.e. efficiency = 1 for all directions and wavelengths.
UseAlternating DOMs	<bool>	0	Alternating placement of downlooking and uplooking DOMs.
UseDoubleDOM	<bool>	0	Proposed PINGU DOMs with two PMTs, one up- and one downlooking.
UseLowEnergy Physics	<bool>	0	Use of Geant4 low energy processes (Compton, gamma conversion, photoelectric effect, Bremsstrahlung, ionisation).
NuMeanEnergy	<double> *<energy>	12.5*MeV	Mean energy of the primary neutrino spectrum, will be converted to the corresponding positron spectrum.
NuSpectrum Parameter	<double>	3.5	Alpha parameter of the primary neutrino spectrum.
UseUnmodified FDSpectrum	<bool>	0	Use the standard Fermi-Dirac neutrino spectrum instead of the modified one. In this case, NuTemperature has to be set.
NuTemperature	<double> *<energy>	6.5*MeV	Temperature of the unmodified FD spectrum. Chemical potential is 0.

3.2.2 Physical Processes

The particles involved in the neutrino reactions in ice are electrons, neutrons, optical photons, and gamma rays along with neutrinos as well as their antiparticles.

The charged light leptons are subject to multiple scattering, ionisation of the surrounding medium, and bremsstrahlung as well as scintillation and the Cherenkov effect. In addition, positrons can annihilate with electrons provided by the surrounding medium.

The bosons that need to be included are optical photons and gamma particles, which are treated as two different particles due to their very different physical behaviour. Gamma particles, which are radiated by the primary positrons, are subject to the photoelectric and the Compton effect and can convert into an electron-positron pair. Optical photons on the other hand are mainly produced in the Cherenkov effect and also via scintillation. As their energies in the eV range are way too low for any particle physics processes, their propagation is governed by absorption and Mie scattering.

Additionally also protons, neutrons, pions, and their antiparticles are included in the simulation as they can be produced at very high energies. If the hadrons are charged, they are also subject to multiple scattering and ionisation, otherwise they can only decay.

All mentioned particles and processes are represented by the corresponding `Geant4` classes in which the physical properties and effects are implemented appropriately [3]. All methods used in this simulation have been tested intensely and have proven to work correctly. The only exception is the Mie scattering class, which is part of the official `Geant4` distribution only since the latest version 9.4.p01, so it could not be tested yet as intensely by the community as the other basic processes.

3.2.3 Detector Geometry

The detector geometry implemented in `I3_Sim` corresponds to the first proposal for a PINGU phase 1 geometry, completely inside IceCube and next to the DeepCore extension. As one can see in Figure 3.1, it consists of 18 strings centred around one existing IceCube string which is not part of the simulation. The string spacing, as well as the DOM spacing on the strings and the depth of the detector in the ice shield, can be chosen freely.

In any case, a rectangular block of ice will be generated as the world volume containing all other structures in a way that a "safety margin" of at least 200 m in every direction is kept from each DOM. This turned out to be necessary as the deep polar ice is so clear that neglecting photons that have been created far from the DOMs actually leads to a significant underestimation of the detector's capabilities.

Vertically 10 m thick ice layers are implemented to take the depth dependence of

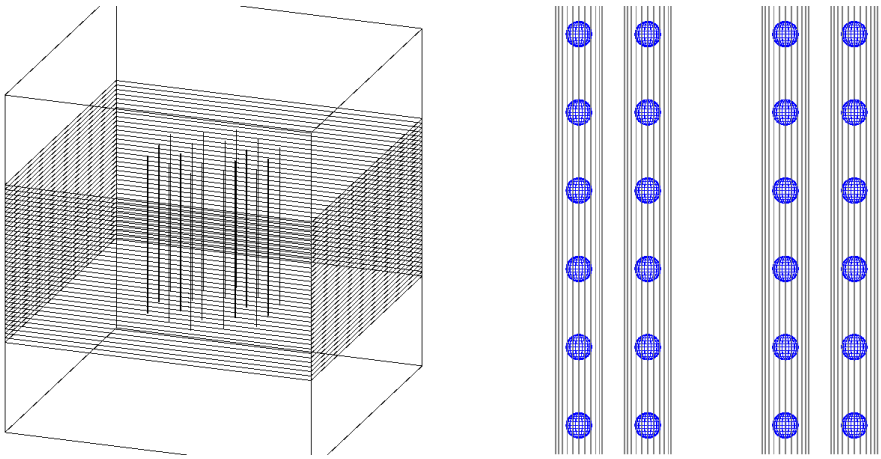

Figure 3.1: *Left:* Complete detector geometry as implemented in `I3_Sim` with 70 m string spacing for better visibility of its features. The horizontal lines in the middle part indicate the 10 m bulk ice layers, the total height of the volume shown is 750 m.
Rigtht: Close-up of the DOMs within the vertical drill holes filled with hole ice.

the ice properties, mainly absorption and scattering length, into account. These are read from a text file that has to be provided by the user and are then assigned to the corresponding layers. This method of reading the ice properties from an external file makes it feasible to easily incorporate different ice models just by exchanging the respective file.

Within each ice layer, 18 drill holes with a diameter of 60 cm that stretch over the whole 10 m high layer are placed in the hexagonal pattern shown in Figure 3.1, sparing the central one that will be formed by an existing IceCube string. These drill holes are filled with so-called hole ice with a substantially lower scattering and absorption length (see Sec. 2.2.2). However, the hole ice has only minor effects on the simulation. The short scattering length does only distort the angular acceptance function which is of no importance for supernova detection, where the typical signature is a homogeneous illumination of the complete detector with almost no directionality. The absorption length of about 40 m should not have any influence in a 60 cm hole. In fact, it turns out the effect is only about 1 % even if the absorption length is decreased to 40 cm.

Distributed evenly within each of the 10 m high hole ice columns there is an integral number of DOMs with a diameter of 13" as in IceCube that form the actual detector. Optionally, so-called double DOMs can be used that were initially

suggested to be installed in the PINGU detector. These consist of two 13" diameter half spheres that are connected by a tube of also 13" diameter and length. Hence the double DOMs could house two PMTs, one upwards and one downwards facing. The actual use of modules of this type is not very probable though, as a recent analysis of the refreezing hole ice showed that dust particles settle down on top of the DOMs, thus obscuring the field of view of a potentially upwards-looking PMT [29].

3.2.4 Generation of Primary Particles

As mentioned above, supernova neutrinos typically have energies in the 5 – 40 MeV range. Due to their extremely low interaction cross-section, computationally it is very ineffective to seed the simulation with neutrinos that in the vast majority only pass the detector without leaving any signal. Thus it is reasonable to only take care of the neutrinos that actually induce an inverse beta decay—which make up more than 90 % of the total detectable signal [5]—and inject the positrons they produce as primary particles.

This is done event by event, which means that in each `Geant4` event only one positron is generated, fully tracked, and processed with all its secondary particles before the next positron is injected in the following event. The energy distribution of the positrons is inferred from the neutrino spectrum that is to be simulated and can be chosen to be either a standard Fermi-Dirac spectrum (1.35) with zero chemical potential or a modified one (1.36).

First a random neutrino energy is picked. Using the respective neutrino spectrum weighted by E_ν^2, which is roughly the energy dependence of the inverse beta cross section (cf. Sec. 1.1.2), and normalized to have a peak value of one, it is decided whether the primary is injected or not by picking another random number between zero and one. If this number is below the value of the renormalised spectral function for the given neutrino energy, the primary is generated, otherwise a new neutrino energy is picked and the check is repeated.

If a certain neutrino energy has passed the above check, the threshold energy (1.3) is subtracted to convert it into the corresponding positron energy. Then the positron is generated at a random position inside the world volume of the simulation. Its momentum direction is also chosen randomly as the directional information of the inducing neutrino is almost completely lost in the inverse beta decay at typical supernova neutrino energies [58]. It has been shown [52] that the remaining directionality might be strong enough to permit a reconstruction of the supernova direction, but as `I3_Sim` is focused on the overall detection capabilities of PINGU, this minor anisotropy is neglected for now (see Sec. 4.2.3 for a discussion).

3.2.5 Implementation of DOM Properties

In principle, the DOMs could be modelled completely within `Geant4`, with full tracking of photons while travelling through their interior. As this has been done before [60], it is more convenient and efficient to just represent the DOMs by solid spheres that correspond to their outer boundary and use the effective quantum efficiency and angular acceptance that have been measured as described in Section 2.3.2. These were implemented differently in the simulation.

As the quantum efficiency neither depends on the specific DOM that has been hit by a photon—at least in a first approximation—nor on the exact point where this DOM has been hit, it does not necessarily need to be applied when a photon actually enters a DOM. In fact, in means of computing efficiency it is way more reasonable to get rid of photons that are not detected as soon as possible to avoid unnecessary tracking, which is the limiting factor of the whole simulation's computing speed.

Hence the implementation works in a way that each time an optical photon is produced by the Cherenkov effect or scintillation, the DOM quantum efficiency at its wavelength is checked via picking a random number in the same way the neutrino spectrum is applied in the primary generation. The tracks that are discarded by this procedure are instantly deleted.

The exact value of the quantum efficiency is calculated from an interpolation of the values tabulated in [60] that lead to the curve in Fig. 2.6 which is then multiplied by 1.35 to take the increased quantum efficiency of the DeepCore DOMs into account [59]. Two additional factors of 0.9 and 0.85 represent the shadowing of the DOMs by various cables that are not part of the simulation and threshold losses due to the PMT's signal waveform, respectively.

By this course of action, more than 90 % of all optical photons are discarded directly after their creation, thus the computational performance is vastly improved. This makes it feasible to process large numbers of events in a reasonable amount of time, even though the generation volume is so large that a lot of primaries are generated far off the detector and have only a small chance to be detected.

The angular acceptance on the other hand can only be applied on the DOM itself. Therefore, first is it necessary that each DOM is registered as an active detector. This means that each time a particle enters the DOM, the `ProcessHits` member function of the sensitive detector class is called. This function checks the identity of the incoming particle and deletes all tracks that do not correspond to an optical photon, i. e. usually electrons, positrons, and gamma rays, that all get absorbed inside the DOM. For optical photons, the zenith angle of their point of entry is retrieved, from which then the angular acceptance is calculated according to (2.1). By evaluating a random number analogue to the implementation of the quantum efficiency it is now ultimately decided whether the photon is detected by the DOM. If yes, a new hit object is created.

3.2.6 Processing of Hits and Output

Each time `I3_Sim` is executed, a new `.root` file is initialised and filled that will contain detailed information about the results that are to be generated.

If a hit is registered, a hit object is created in which all information about this hit is stored. This information includes, in that order:

EvtID The number of the event in which the hit occurred

HitNoInEvt The number of the hit in the event, i. e. if this was the first, second, third, ... hit that this single positron produced

StringNo The number of the string (0 – 17) on which the hit was registered

DOMNo The number of the DOM (counted from the bottom of the string) on which the hit was registered

x_Hit, y_Hit, z_Hit The x, y, and z coordinates of the point where the photon entered the DOM in m

t_Hit The time stamp of the hit in ns (zero is defined by the injection of the primary)

DistToPrim The distance between the location of the hit and the primary positron's injection point in m

wvl_phot The wavelength of the registered photon in nm

x_Prim, y_Prim, z_Prim The x, y, and z coordinates of the point where the primary positron was injected in m

px_Prim, py_Prim, pz_Prim The x, y, and z components of the primary's momentum in MeV/c

The information of all hits is stored as a `ROOT` NTuple named "Hit Collection" which is simply a table of numbers in double precision that makes it easy to histogram the stored quantities [16]. Additionally, for each hit, the zenith angle of the primary positron at its injection point is stored in an histogram called "Primary zenith angles". Also the position injection point is stored in two scatter plots named "Primary positions from top" and "Primary positions from side" as they are projections on the xy and xz planes, respectively. Of course these quantities could also be retrieved directly from the Hit Collection, but as they are useful as quick test of the correctness of the simulation they are always created by default.

If a hit was the second one to be registered in one event, i. e. when `HitNoInEvt` $= 2$, the time difference and the spatial distance to the first one will be calculated and plotted in two histograms called "Time" and "Distance", respectively. Both are

also plotted against each other in a scatter plot called "MultiHit Time-Distance Correlation". These plots will be helpful for finding adequate coincidence windows for multiple hits.

Once the processing of an event is completed, a summary of it is stored in another NTuple called "Event Collection" that contains the following quantities:

TotalHits The total number of all hits that have been registered in this event

DOMsHit The number of different DOMs that have been hit

DOMsDoubleHit The number of different DOMs that have registered more than one hit

If, for example, in one event there was one photon registered in DOM A, two in DOM B, and one in DOM C, `TotalHits` is four $(1+2+1)$, `DOMsHit` is three (DOMs A, B, and C), and `DOMsDoubleHit` is one (only DOM B).

Apart from the registered hits, additional quantities are stored to monitor the correct behaviour of the simulation. These are the histograms "Primary Energy" in which the energy of each primary positron is recorded and "Photon Wavelength" which does the same for the vacuum wavelength of all optical photons that are produced in the simulation, predominantly by the Cherenkov effect.

Finally there are two scatter plots for the close monitoring of the Cherenkov effect. In the first, called "Photon Production", the total number of photons that have been produced in an event is plotted against the initial energy of this event's primary positron. In the "Positron Track Length" plot the summed total track length of all positrons and electrons above the Cherenkov threshold is plotted against the primary energy. Although this quantity is dominated by the track of the primary positron, it also accounts for secondary tracks of secondary electrons and positrons originating from gamma particles that were created as bremsstrahlung and then converted into a lepton pair again. This is guaranteed by the way the track length is measured: For each step that is processed in the simulation first it is checked if the corresponding particle is either a positron or an electron. If this is true, the total energy of this particle is queried. If the energy is above the Cherenkov threshold of 783 keV[1], the length of this step is added to the track length variable which, after processing the whole event, enters the plot and is reset to zero afterwards.

The `.root` files produced by `I3_Sim` are rather complex as one can see from the above description of their structure and hence not capable of giving a quick overview of the outcome of a given run. Also they do not contain any information about the simulation settings, so that a `.root` file without the corresponding settings file would be useless. For this reason, an additional `.out` output text file of the same name as

[1] This is the sum of a electron's or positron's rest energy of 511 keV and the kinetic energy of 272 keV resulting from the Cherenkov condition, see Sec. 1.1.3

the `.root` file is written. It contains the detector and neutrino spectrum settings along with some analysis results.

The analysis provides the active volume of the detector for different trigger conditions that are defined by the way hits are counted and by the number of DOMs that have been hit. The active volume is a measure of the ability of the detector to detect an event by initiating this trigger. It is defined by

$$V_{act} = \frac{\text{triggered events}}{\text{total events}} \cdot \text{generation volume} \tag{3.1}$$

For better comparability of different detector configurations, in the `.out` files the active volume is given per DOM.

As the contents of the `.out` files are mostly self-explanatory, only an example is given below.

```
Detector Settings:
  Lower boundary of detector (I3 coordinates): -505.0 m
  Height of detector:                          350.0 m
  Number of ice layers:                        35
  String spacing:                              5.00 m
  DOM spacing on strings                       1.00 m
  Total number of DOMs:                        6300
  Use perfect DOMs (i.e. 100% efficiency):     false
  Alternating DOM direction:                   false
  Use DoubleDOMs:                              false
  Use low energy processes:                    false

Primary Generator Settings:
  Randomized primary position:                   true
  Use primary neutrino spectrum:                 true
 Using modified Fermi-Dirac spectrum
  Mean energy of primary neutrino spectrum:      12.47 MeV
  Alpha parameter of primary neutrino spectrum:  2.84


Run Statistics:
  Number of primaries generated:         1000000
  Mean positron energy:                  17.23 MeV
  Number of hits registered:             33159


Analysis Results: (Active Volume per DOM for this event class)
  Total Hits seen:                          6.963e+02 +- 3.824e+00 m3
  Total Events seen:                        4.976e+02 +- 3.233e+00 m3
  Total Events with more than one hit:      9.223e+01 +- 1.392e+00 m3
  Total MultiHits in same DOM:              6.027e+00 +- 3.558e-01 m3
  Events with MultiHits in same DOM:        5.061e+00 +- 3.260e-01 m3
  Events with hits in two or more DOMs:     9.179e+01 +- 1.388e+00 m3
  Events with hits in three or more DOMs:   3.860e+01 +- 9.003e-01 m3
  Events with hits in four or more DOMs:    2.106e+01 +- 6.651e-01 m3
  Fraction of MultiHits on same DOM:        0.881 +- 0.052 %
```

The entries in the analysis results are defined in the following way:

Total Hits seen All hits on every DOM are counted without any restriction. This corresponds to the sum of all `TotalHits` in the Event Collection. In principle, this could lead to a total active volume that is larger than the generation volume as the mean number of hits per event could be more than one. Practically this is not the case due to the wide "safety margin" of 200 m around the detector.

Total Events seen Each event for which at least one hit was registered is counted once. Thus in this case the number of triggers can never exceed the number of events and the total active volume is always smaller than the generation volume.

Total events with more than one hit All events for which `TotalHits` is greater than one are counted once. No distinction is made whether these hits were registered on the same or on different DOMs.

Total MultiHits in same DOM All DOMs are counted that have been hit at least twice in a single event. This corresponds to the sum of all `DOMsDoubleHit` in the Event Collection, which can be greater than one for one event.

Events with MultiHits in same DOM The same as above, but now each event for which `DOMsDoubleHit` is non-zero is counted only once.

Events with hits in two/three/four or more DOMs Each event is counted once, for which `DOMsHit` is at least two, three, or four, respectively.

Finally, the "Fraction of MultiHits on same DOM" is calculated as the ratio between the sum of all `DOMsDoubleHit` and the sum of all `DOMsHit` in the Event Collection.

4 Analysis

In this chapter, first some cross-checks of the correct running of `I3_Sim` will be described. Then the behaviour of the PINGU detector for different configurations and its response to variations of the neutrino spectrum is analysed with special regard to the detection of multiple hits, as this could be the key to a significant reduction of detector noise. Based on this, coincidence cuts for the detection of multiple hits are proposed and a noise estimate using these constraints is given. Finally the signal estimations for different supernova models will be shown for PINGU compared to those of the existing IceCube detector.

4.1 Consistency of `I3_Sim`

Following the subsequent steps in the simulation, one first has to check whether the spectrum of the primary positrons is implemented properly. As can be seen from Figure 4.1, the positron spectrum generated by `I3_Sim` nicely fits the prediction resulting from weighting the neutrino spectrum with E^2 and applying the threshold function (1.3).

The linear relationship between the primary's energy and its full track length above the Cherenkov threshold including secondaries has already been shown and discussed in Section 1.1.3. The few entries in Fig. 1.4 whose track lengths are significantly below the mean can be explained by primaries that have been produced very close to either a DOM or the outer boundary of the simulated volume.

This linearity is conveyed to the production of Cherenkov photons, which has also been pointed out before (Sec. 1.1.3). However, a discrepancy between the Cherenkov photon production rates calculated from the Frank-Tamm formula (1.25) and that retrieved directly from the simulation was found.

One reason for this is the finite simulation step length of the particles that radiate Cherenkov photons. As the Cherenkov effect is a continuous process causing only minor energy loss, the emission of Cherenkov photons is implemented in a way that it happens during the particle's steps without changing its state. The step length is by default only modified by the other effects the particle is subject to. However, the step length can be restricted to a specified mean number of Cherenkov photons per step by an additional option so that the modelling of the Cherenkov effect becomes more accurate. This mean number of Cherenkov photons per step has been set to 30 in `I3_Sim`, which still leaves some uncertainty in the total number of produced

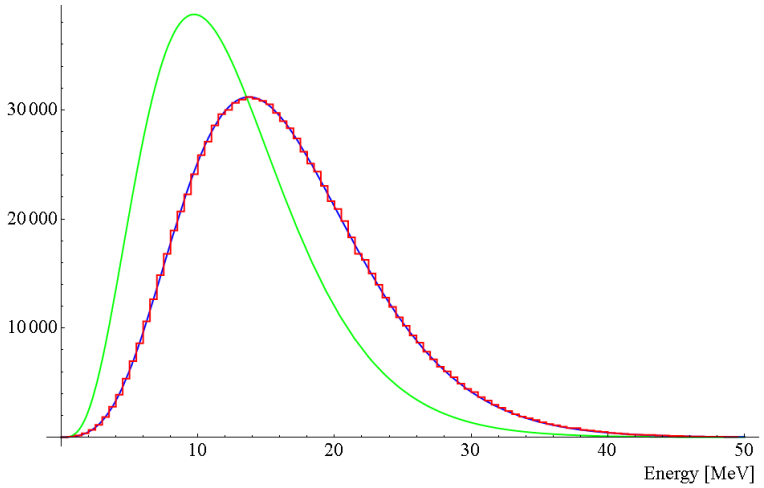

Figure 4.1: Modified Fermi-Dirac neutrino spectrum (1.36) with $\langle E_\nu \rangle = 12.5\,\mathrm{MeV}$ and $\alpha = 3.5$ in green and the resulting positron spectrum in blue. In red, a histogram of one million positrons generated by `I3_Sim` for the same neutrino spectrum is shown. The relative scale between the three is arbitrary and was chosen to give the best comparability.

photons. This uncertainty could be reduced by further decreasing the mean number of photons per step, but the observed discrepancy of about 3 % is already larger than the influence of the step length, which can be estimated to be

$$\Delta_{\text{step length}} = \frac{\text{production limit per step}}{\text{mean total number of Cherenkov photons}} = \frac{30}{3600} \approx 0.8\,\% \qquad (4.1)$$

at a positron energy of 20 MeV.

A larger influence on the Cherenkov photon production is due to the fact that the calculated number of generated photons per track length (1.24) is based on a mean refractive index of polar ice not taking into account its dispersion. In the simulation on the other hand, group and phase refractive index are read from the ice table that is provided and therefore—at least for the ice model that was used throughout the work connected to this thesis—do include wavelength dependent refractive indices.

The dispersion in ice becomes obvious when looking at the spectrum of Cherenkov photons generated by `I3_Sim`. As one can easily see from the wavelength dependent version of the Frank-Tamm formula (1.23), the spectrum should be proportional to $1/\lambda^2$ if all other quantities are constant over the considered wavelength interval. However, Figure 4.2 clearly shows an excess at small wavelengths that is a result of the refractive index decreasing with λ.

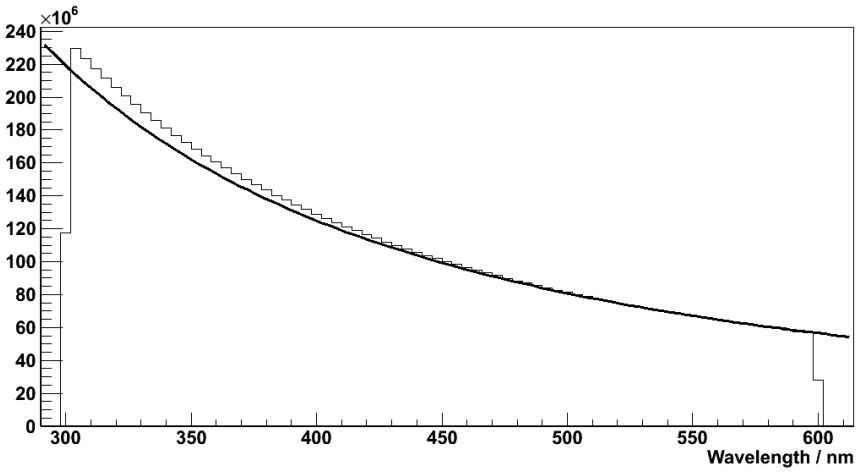

Figure 4.2: Cherenkov photon spectrum produced by `I3_Sim`. For comparison, the solid black line shows an exact $1/\lambda^2$ spectrum.

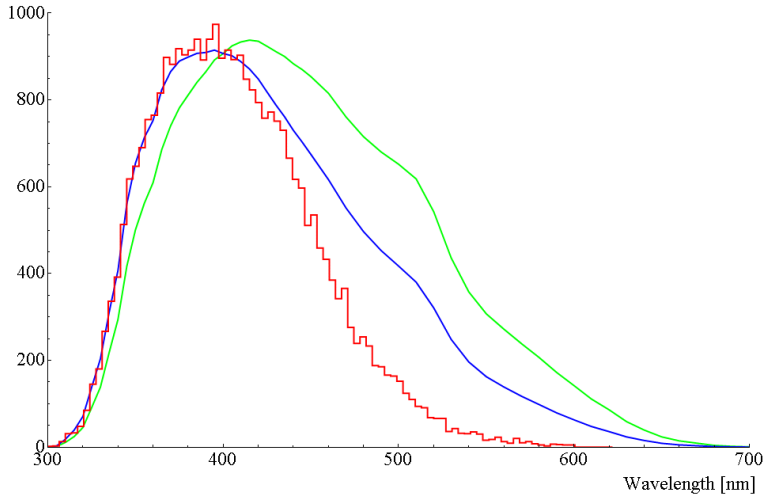

Figure 4.3: The DOM quantum efficiency according to measurements [60] and weighted by $1/\lambda^2$ in green and blue, respectively. In red, the photon spectrum seen at the `I3_Sim` DOMs is shown. The relative scale between the three is arbitrary and was chosen to give the best comparability.

The next point to investigate is if the DOM properties are modelled correctly. The photon spectrum detected by the DOMs should resemble their quantum efficiency function weighted by $1/\lambda^2$, taking the form of the Cherenkov photon spectrum into account. Although the Cherenkov photon spectrum generated in `I3_Sim` actually shows an excess of photons with short wavelength as stated above, this is not able to explain the significant overestimation of the detected spectrum that can be seen in Figure 4.3 for wavelengths above about 400 nm.

The reason for this is the absorptivity of the polar ice that starts to increase rapidly at about 400 nm while being rather constant below this value. Thus the reddish part of the photon spectrum suffers much more absorption and is thinned out before even reaching the DOMs.

Finally, one can take a look at the distribution of the primaries that have been detected. As they are generated completely randomly in position and direction, effects of the detector configuration should be visible when examining their initial kinetic conditions.

The direction of the injected positrons is, as stated above, completely random. If the DOMs did not have any directionality, the same would be true for the fraction of the positrons that are detected via the Cherenkov photons they emit. Therefore, plotting their zenith angles should give a sine-like distribution resembling the $\sin\vartheta$ weighting factor of the surface differential in polar coordinates.

However, as one can see in the left panel of Figure 4.4, in the actual distribution small zenith angles—which correspond to upwards moving positrons—are preferred. This is not surprising as the DOMs in fact do have a directionality due to their downwards facing PMTs. A simple weighting of the primaries' directional distribution with the angular acceptance of the DOMs (2.1), does not describe the detected distribution either, rather the result is between both. The reason for this is that this two curves mark only the extreme cases of no and full application of the DOM directionality. The maximum anisotropic case is not reached for the the following reasons:

First, in Fig. 4.4 shows the zenith angles of the primaries are plotted while Cherenkov photons are radiated at the Cherenkov angle of 41 °(1.19). Second, the direction of the positrons can vary along their path through the ice due to multiple scattering. Finally the photons can be scattered, too, especially inside the refrozen drill hole ice around the DOMs, which has a reduced scattering length of only 40 cm compared to typically more than 100 m in the surrounding bulk ice.

Considering the injection positions of the detected positrons, one sees that the number of detections decreases with increasing distance as one would expect (Fig. 4.4, right). However, due to the large absorption length in the ice this decrease is rather weak so that one still has a contribution from distances above 200 m. As this fraction is small, the choice of an only 200 m "safety margin" around the detector can

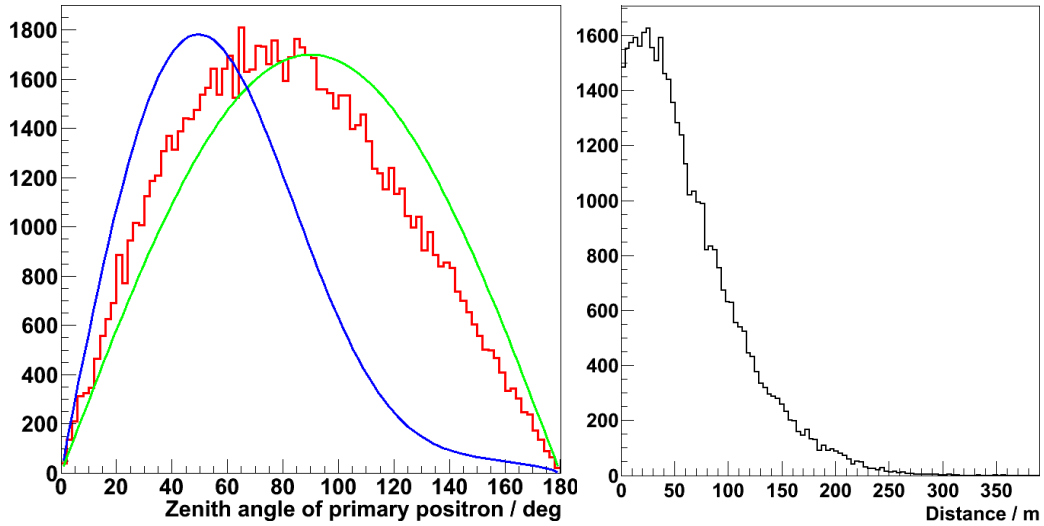

Figure 4.4: *Left:* Zenith angles of primary positrons that have been detected via their Cherenkov light (red), a simple sine function (green), and a sine weighted with the angular acceptance of the DOMs (blue).
Right: Distance between DOMs registering a photon and the point where the corresponding primary was generated.

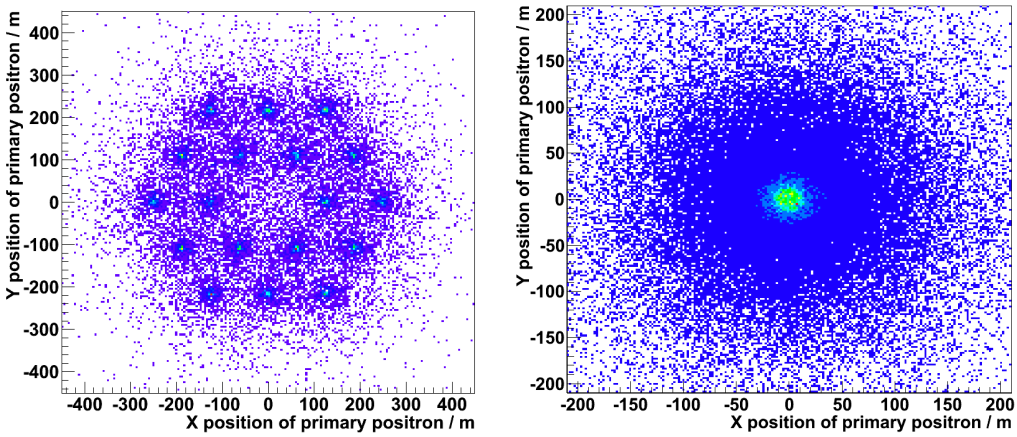

Figure 4.5: Top view of the initial positions of the detected positrons for 125 m (left) and 5 m (right) string spacing.

be justified[1]. However, it is clear that this margin should not be decreased much further because this would significantly reduce the number of detected photons and hence underestimate the detector's active volume.

This distance distribution of the hits relative to their primaries suggests that the detection probability of a positron is enhanced in the vicinity of a DOM. This effect can in fact be seen for a sufficiently large string spacing, where the positions of the strings are clearly visible when looking at a top view plot of the detected positrons' initial positions, see Figure 4.5 (left). For closer configurations with a string spacing of only a few metres, which are intended for the future PINGU detector, the string structure is not longer visible (see Fig. 4.5 right) due to the large width of the distribution in figure 4.4 (right).

4.2 Optimisation of PINGU for Supernova Detection

4.2.1 Detector Configuration

The first goal in optimising PINGU phase 1 for the detection of galactic supernovae is finding the most suitable detector configuration. Therefore a series of `I3_Sim` simulations was run in which a number of different string and DOM spacings were tested. In the process, the string spacing was varied between 5 m and 35 m for a DOM distance of 1 m, 2 m, 5 m, and 10 m with one million events each produced according to a modified Fermi-Dirac neutrino spectrum (1.36) with a mean energy of 12.47 MeV and $\alpha = 2.84$.

This choice, corresponding to the time integrated neutrino spectrum of a supernova with a $8.8\,M_\odot$ progenitor star [28], is rather conservative and marks the lower bound of the energy range in which estimates of supernova neutrino spectra usually are located. Thus the values of the active volumes that are the results of the `I3_Sim` runs can be seen as very conservative estimates as one would expect the active volume to increase with the mean neutrino energy. A closer look at the energy dependence of PINGU's detection capabilities will be taken in Section 4.2.2.

The active volumes for the most important trigger conditions that are also stored in the `.out` files created for each run are shown in Figure 4.6, each plotted as a function of the string spacing.

One can see that the active volume for counting all hits in the detector (top left) is nearly constant between $700\,\mathrm{m}^3$ and $800\,\mathrm{m}^3$. This value can be interpreted as the volume around each DOM within which all generated positrons are detected when neglecting multiple hits on the same DOM. As this quantity treats the DOMs completely separately, it should not depend on their position relative to each other.

[1] Note that the number of potential DOMs that can be hit increases roughly with the square of the distance as long as it is not much larger than the diameter of the detector. The probability that a particular DOM registers a hit thus corresponds to Fig. 4.4 (right) divided by distance^2.

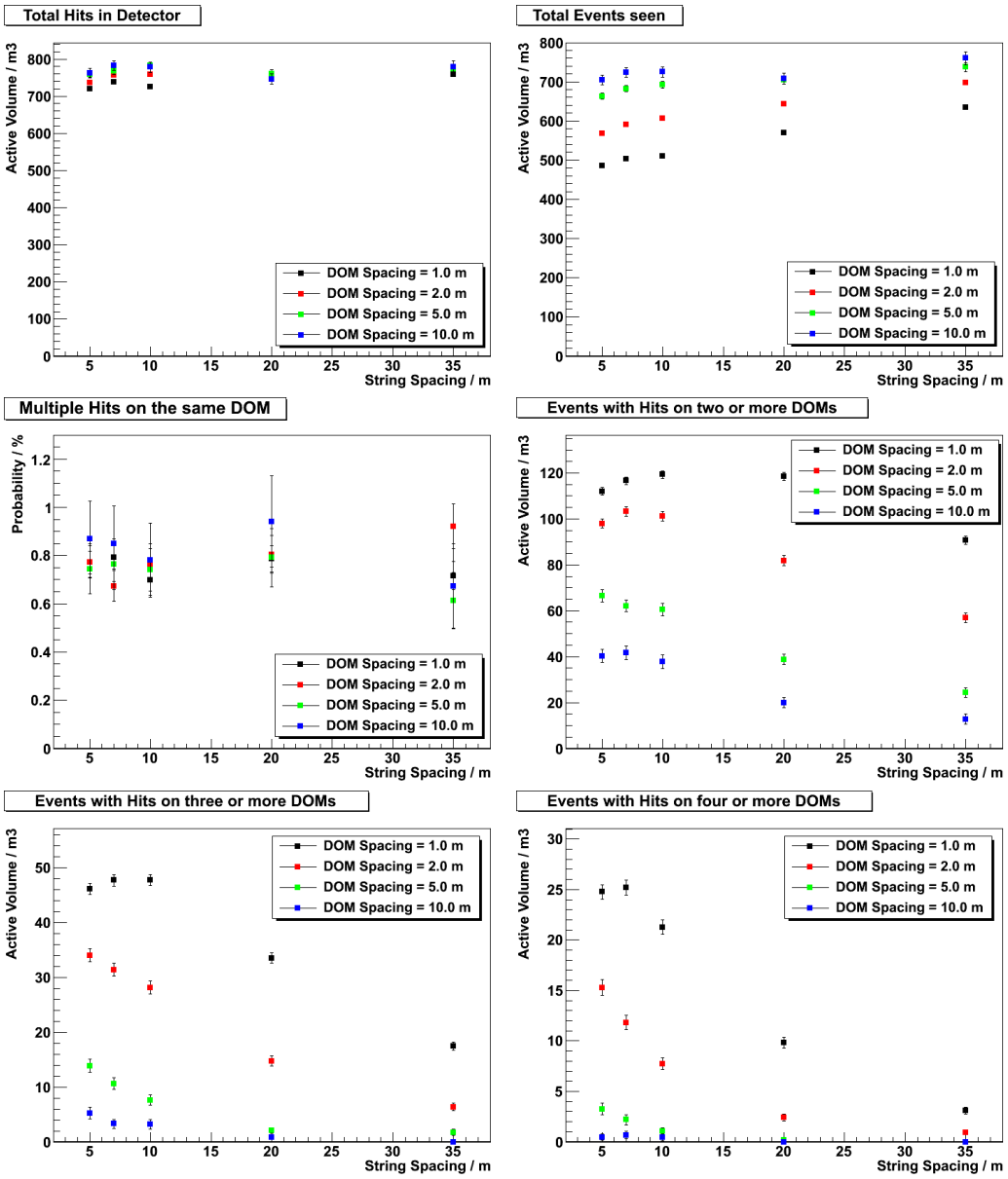

Figure 4.6: Active volumes of PINGU for different detector configurations. All active volumes are given per DOM.

The slight dependency on the string spacing is a result of the generation volume increasing with the string spacing. As discussed above, the "safety margin" of 200 m between detector and the boundary of the generation volume is only just sufficient, in fact photons can reach a DOM even when they originate from a positron generated more than 200 m away. So some of the possible hits are cut by these boundary effects, but their influence reduces as the generation volume grows. In addition, in the most dense configurations the shadowing of a DOM by the surrounding ones cannot be neglected any more which of course decreases the amount of photons the DOMs can collect.

When only counting each registered event once, regardless of how many hits have been detected in the event, the active volumes are reduced for close detector configurations (top right). At first sight this is confusing, but in fact this quantity is a measure of the active volume of the whole detector divided by the number of its DOMs without double-counting the overlapping parts of the individual DOMs' active volume. Therefore the configurations with the widest DOM spacing and hence the fewest overlap are least affected when comparing these values to those where the DOMs are treated independently. As expected, this effect lessens with increased string and DOM spacing.

The probability of registering more than one hit in one event on a single DOM (middle left) is slightly below 1 % for all simulation runs. This means that when a DOM has been hit, there is a chance of 1 % for it being hit again by at least one additional photon originating from the same primary. Here the DOMs are treated separately again, so it is no surprise that this probability is independent of the detector setting. This possibility of DOM registering more than one hit from the same interaction has—in principle—to be taken account of when calculating the total active volume per DOM. In the actual experiment, however, one has no possibility to decide whether two subsequent hits in a DOM do belong to the same or different positrons, so the downscaling becomes irrelevant.

Finally there are three plots shown for events that generate hits on at least two, three, and four DOMs from middle right to bottom right. For choosing the PINGU configuration suited best for supernova detection, these are the most relevant plots, as the noise can be reduced significantly if coincidences on several DOMs are required. The reason that this is not yet done in IceCube is its widely spaced design with correspondingly low coincidence rates for MeV events [11].

This is reflected in the fact that—at least as a general trend—the active volumes for coincidences drop when the PINGU configuration is changed to a wider arrangement of the DOMs. For double coincidences, one can see that the DOM spacing on the strings is the most important factor while the string spacing has only minor influence. In fact, for the very small DOM spacings of 1 m and 2 m the coincident hit volume actually rises between 5 m and 10 m string spacing. This is due to the same effect of reducing the overlap of the individual effective volumes that was discussed above.

When the requested hit multiplicity is increased, the string spacing becomes more important, but in any case the effect of the DOM spacing stays dominant. Also, as one would naturally expect, the active volumes are becoming more sensitive to the separation of the DOMs for a higher hit multiplicity. Thus the detection of triple or even quadruple hits is only reasonably possible in the very dense configurations.

The optimum seems to be at 1 m DOM spacing, which is the closest possible, and 7 m or 10 m string spacing, which is wide enough for the "overlapping volume effect" to die out and close enough to keep most of the active volume for triple or higher coincidences. For the further study of coincidences in Section 4.2.4, a string spacing of 10 m will be assumed.

4.2.2 Energy Dependence

The track length and hence the amount of Cherenkov photon production of positrons in ice is strongly correlated and in fact directly proportional to their energy, as it was shown in Section 1.1.3. Therefore, also PINGU's active volumes should show this dependence. This was examined for the closest possible configuration, i. e. 5 m string and 1 m DOM spacing, by performing a series of `I3_Sim` runs where the mean neutrino energy was tuned between 12.5 MeV and 30 MeV in steps of 2.5 MeV. The spectral parameter was kept at $\alpha = 3.5$ as it does not change the mean neutrino energy and has only a minor effect on the resulting mean positron energy.

The plots of the active volumes for the same trigger conditions as in the previous section are shown in figure 4.7, but now as functions of the mean neutrino energy. The total active volume for each DOM independently (top left) scales nearly exactly linearly with the neutrino energy as one would expect. The minor deviation from exact linearity is probably an artefact of the threshold function for inverse beta decay and its cross section that rises with E_ν^2, which make the relation between mean neutrino and positron energy slightly non-linear.

When counting events, the active volume shown in the top right plot only scales like $\langle E_\nu \rangle^{0.75}$. This is again an effect of the overlapping volumes of the individual DOMs. Since these volumes grow with increasing energy, the overlapping fraction also grows. Hence the non-overlapping part that is measured by this quantity cannot increase as fast as the individual volumes.

The fraction of multiple hits also increases with energy simply because the positrons produce more light. The exact functional relation, however, is more complicated than a simple power law because the directions of photons generated by the same positron are strongly correlated due to the Cherenkov cone condition. As the relative errors in this plot are rather large, the relation does not become evident. One would have to go to much higher energies and statistics for a more precise analysis.

When it comes to the active volumes for multiple hits, one would naively expect

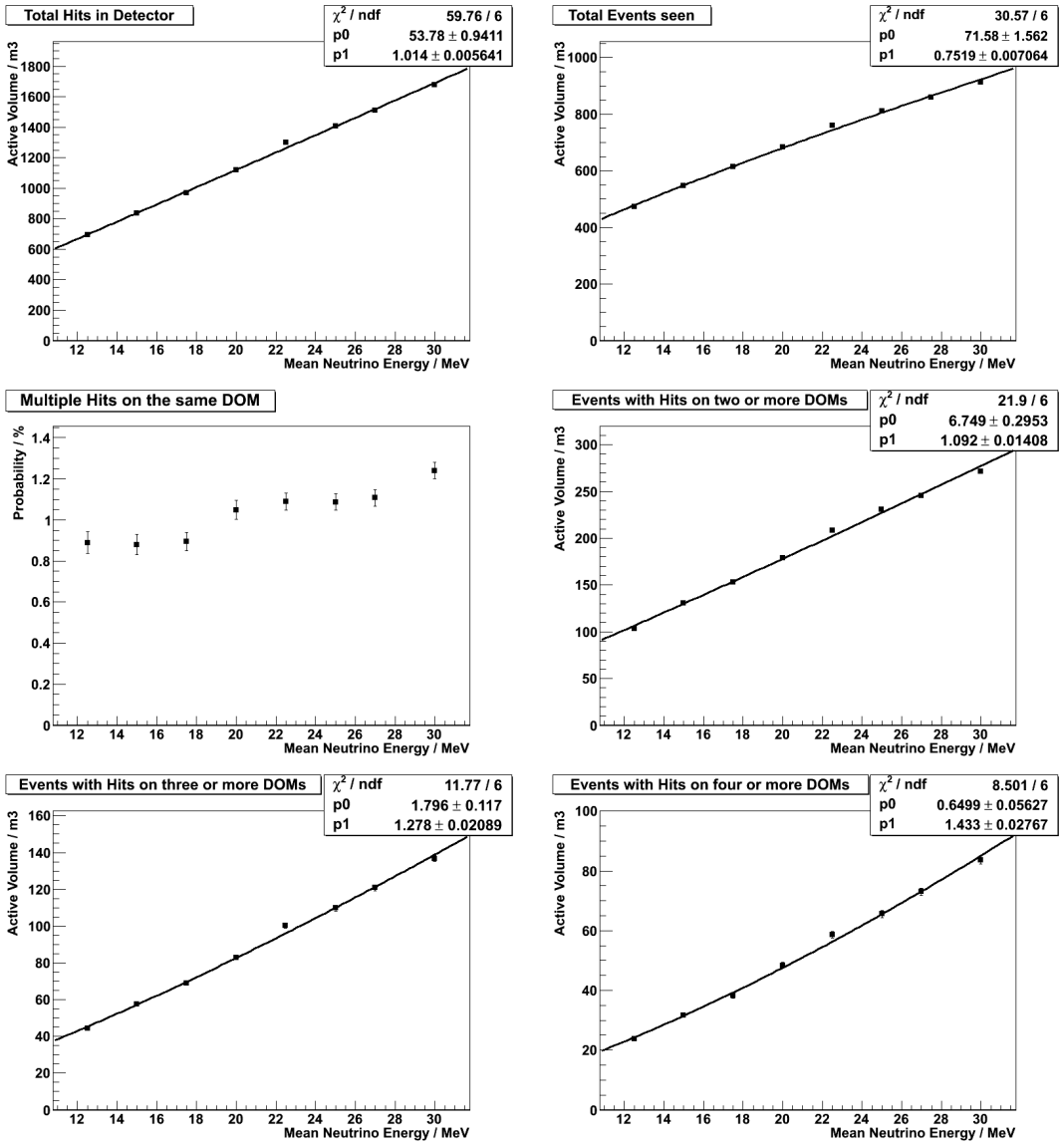

Figure 4.7: Energy dependence of PINGU's detection capabilities, given as active volumes per DOM. All fits use a power law model of the form $y = \mathtt{p0} \cdot x^{\mathtt{p1}}$.

that those scale roughly like the mean neutrino energy raised to the n-th power when an n-fold coincidence is required. This follows from the rather natural assumption that once a positron generates an Cherenkov photon in the ice, there is some probability p that this photon will be detected by a DOM. Hence the probability that a photon is detected in this event is p multiplied with the number of photons that were generated.

If one now requires that at least two different DOMs are triggered, the probability for this should just be the square of the above probability as the two DOMs are independent from each other. The Cherenkov cone that had to be taken into account for the probability of multiple hits on the same DOM should not have an effect in this case as the DOMs are required to be different and their configuration is sufficiently dense.

As PINGU in the proposed geometry will have sufficient detection capabilities for double and higher coincidences it is possible to count their rates separately. Due to their different scaling with energy, it should be possible to obtain a relative measure of the mean neutrino energy from the ratios of these rates. When observing a supernova, the neutrino energy changing with time as the collapsing star's core cools down can be traced, adding a whole new observable to the recorded information.

However, when looking at the actual numbers in Figure 4.7, the observed energy dependence is much weaker, making it difficult to extract of the neutrino energy from the coincidence rates. The energy dependence increases though, but only from $\langle E \rangle^{1.09}$ for double to $\langle E \rangle^{1.43}$ for quadruple coincidences instead of $\langle E \rangle^2$ to $\langle E \rangle^4$ as expected. A discrepancy this big is surprising at first sight and needs to be explained.

The explanation is that not all positrons can be treated equally. In fact one has to distinguish between those that are generated in the very centre of the detector where they are densely surrounded by lots of DOMs, and those starting their track far off the instrumented area in the bulk ice. To analyse this, `I3_Sim` was run twice in the closest possible setting, the first time only generating positrons at positions that were inside the grid of DOMs. In the second run, the positrons were generated exclusively outside this volume.

The latter ones show a much stronger energy dependence as was observed before without restrictions on the primary positions, which can be seen from the left column of Figure 4.8. They still do not show the proportionality to E^n with n being the requested multiplicity that comes out of the above estimate, but the different multiplicities are much clearer separated.

For positrons generated inside the grid of DOMs it is the other way around, the dependence on the neutrino energies is now even less than before. This is due to a saturation effect that kicks in for this close detector configuration: Even rather low energy positrons will produce some 10^3 Cherenkov photons so that it is very likely to trigger more than one DOM. Of course the probability of triggering multiple DOMs still increases with energy, but with several thousand photons present in the centre

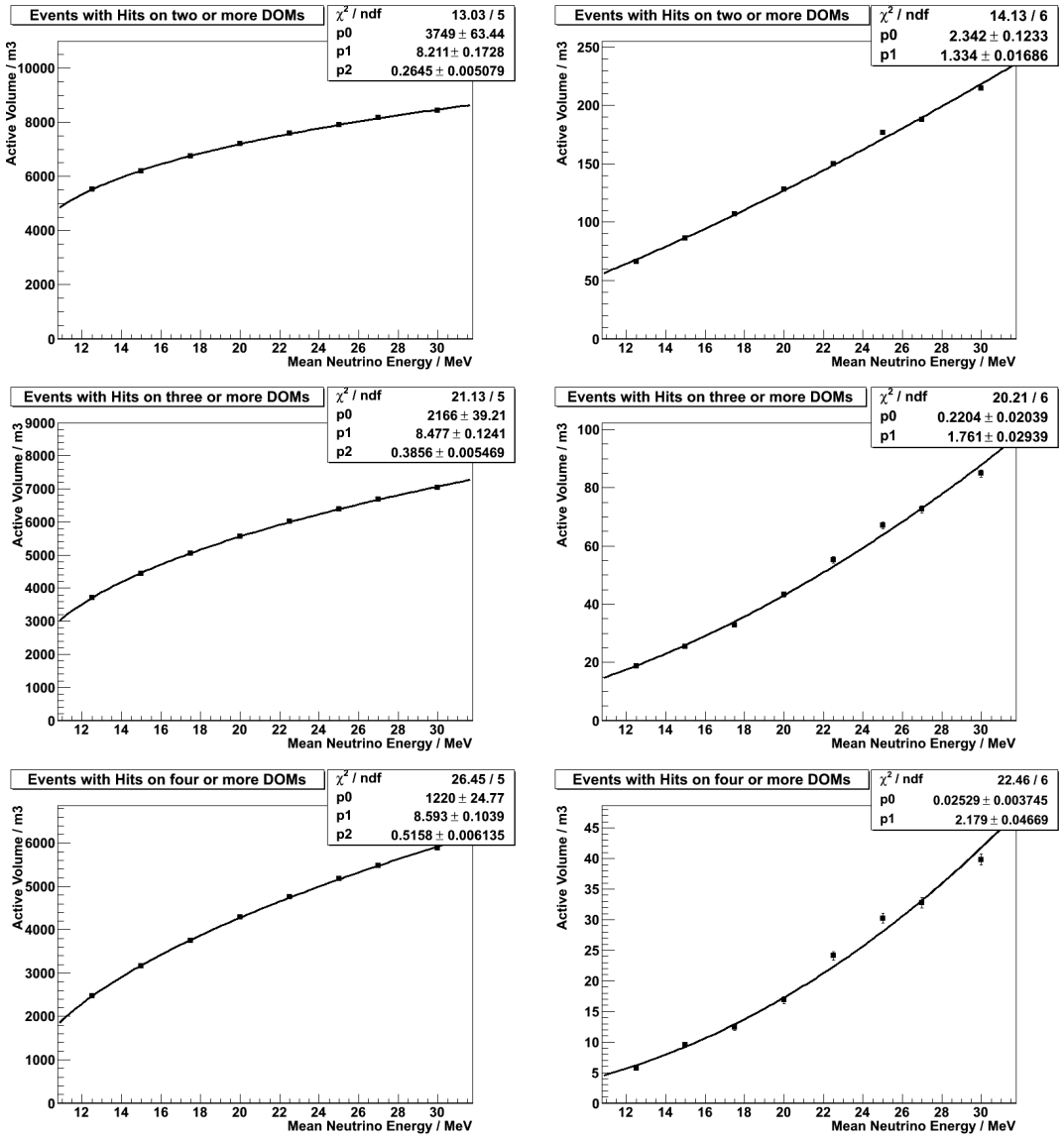

Figure 4.8: Energy dependence of PINGU's multiple hit volumes for primaries generated inside (left column) and outside (right column) a 10 m margin around the outermost DOMs. The fits for the positrons generated outside the detector use a power law model of the form $y = \mathtt{p0} \cdot x^{\mathtt{p1}}$ as above, while for the positrons inside the detector a modified model $y = \mathtt{p0} \cdot (x - \mathtt{p1})^{\mathtt{p2}}$ was used.

of the detector in any event, their number and hence the primary's energy is not that important any more and factors like the geometry of the Cherenkov cone gain weight.

Another hint for this saturation are the absolute scales of the active volumes for different coincidence multiplicities in both cases. For the distant positrons, at 12.5 MeV the active volumes for double and quadruple hits are $66.4\,\mathrm{m}^3$ and $5.6\,\mathrm{m}^3$, respectively, which is a difference of almost a factor 12; at 30 MeV they are still separated by a factor $215\,\mathrm{m}^3/40\,\mathrm{m}^3 \approx 5$. When restricting the generation volume to the inner part, however, the same active volumes vary between $5500\,\mathrm{m}^3/2500\,\mathrm{m}^3 \approx 2.2$ and $8400\,\mathrm{m}^3/5900\,\mathrm{m}^3 \approx 1.4$[2].

In reality of course only the photons hitting the DOMs can be counted and it is not possible to determine the interaction vertex if only a few hits are registered. Hence the only rates that are available experimentally are the ones shown in Figure 4.7 which are dominated by the close positrons, making it more difficult to determine the neutrino energies.

As for a very dense PINGU geometry positrons generated within the detector are rather likely to trigger a large number of DOMs, it might be feasible to aim at very high multiplicities in the order of five to ten triggered DOMs in order to achieve a much cleaner signal by reconstructing event vertices and possibly positron directions. The prospects of this approach have been discussed in [36].

4.2.3 Directionality

IceCube in the recently completed full configuration and even more PINGU provides the best statistics in case of a nearby supernova, i. e. it will have by far the highest count rates of neutrino events of all comparable experiments. However, as it only records count rates and is not able to reconstruct positron tracks, up to now it cannot provide any directional information. Yet this information would be most precious, especially if extracted in real time, because the neutrino signal of a supernova will arrive several hours before the optical one and thus give an advance warning for optical telescopes. Any help for pointing the telescopes at the right spot would dramatically reduce the fraction of the sky that has to be monitored for the optical counterpart.

PINGU will have some anisotropy in its design since all DOMs are installed with the PMTs facing downwards. So one would expect that it is more sensitive to photons and hence also positrons that come from below than to those from above. In principle, it should be possible to infer the zenith angle of a supernova from this as it was already discussed for IceCube in [52].

[2]Note that the absolute values of the active volumes are misleading, especially for the positrons inside the detector, as the complete simulated volume was still considered for their calculation.

Therefore `I3_Sim` was run for a PINGU geometry with 10 m string and 1 m DOM spacing and a modified Fermi-Dirac neutrino spectrum with $\langle E_\nu \rangle = 12.5\,\mathrm{MeV}$ and $\alpha = 3.5$ for strictly upwards and downwards going positrons. For means of comparison, also a run with the same settings but randomly oriented positrons was made. A summary of the results is shown in the table below.

Table 4.1: PINGU sensitivity for upgoing and downgoing positrons compared to random orientation. Here, "n DOM events" means the number of event in which at least n DOMs have registered a photon.

	Downgoing	Upgoing	Random
Total active volume per DOM	$620(4)\,\mathrm{m}^3$	$777(4)\,\mathrm{m}^3$	$693(4)\,\mathrm{m}^3$
Two DOM events / All registered hits	15.0(3) %	16.5(2) %	14.9(2) %
Three DOM events / All registered hits	4.85(13) %	7.18(15) %	6.39(14) %
Four DOM events / All registered hits	1.64(8) %	3.57(10) %	3.42(10) %
Fraction of multiple hits on the same DOM	0.32(4) %	1.26(6) %	0.90(3) %

As one can see, the total active volume depends on the positron direction as was expected. Positrons moving upwards will produce 25 % more hits than those in the opposite direction. In fact, from the angular acceptance function of the DOMs (see Fig. 2.7) one would infer an even stronger dependence. But due to photon scattering, especially in the refrozen drill hole ice directly around the DOMs with its short scattering length, the effect is weakened significantly.

However, the different total active volumes for upwards and downwards moving positrons alone do not allow the reconstruction of the supernova direction as one does not know the absolute neutrino flux passing through the detector with sufficient precision. Therefore one needs to consider ratios of different count rates which are also shown in table 4.1 where the number of events that triggered at least two, three, and four DOMs was put in relation to the total number of hits. These numbers show that for triple coincidences the ratio to the total count rate varies by almost 50 % from zero to 180° zenith angle, while for quadruple coincidences it actually doubles.

Also the fraction of multiple hits on the same DOM was calculated as described in Section 3.2.6. This quantity also shows a variation by a factor four, but it will not be as easy to extract as the ratios of the count rates because in IceCube it has been observed that the DOMs show intense correlated noise [24], which is not discernible from two subsequent photon hits generated by a single positron.

Thus the most straight-forward method to observe the direction of supernovae will be the comparison of the rates for multi-DOM coincidences. However, only the

neutrinos will point along the line of sight towards its position in the sky. The positrons are secondary particles generated via the inverse beta decay whose direction is correlated only very slightly to the neutrino direction at typical supernova neutrino energies (see Sec. 1.1.2). In addition, this correlation varies with the neutrino energy.

So one has to know the mean neutrino energy to calculate the supernova direction, which unfortunately is also carried out via the ratios of the different coincidence rates as described in the previous section. To disentangle the directional from the energetic variation of the rates will be a very delicate task. A possible approach could use the fact that the mean neutrino energy is time dependent while their direction is, of course, constant. Also the rates will be very high and hence have small statistical errors. Additionally, the count rates of the detector before the onset of the supernova are also recorded so that by subtracting them the background can be discarded and detector related asymmetries can be accounted for.

Summarising one can say that, in principle, the reconstruction of the supernova direction and energy should be possible. Although promising first results for IceCube have been shown in [52], further studies are necessary to estimate the prospects.

4.2.4 Possible Cuts and Noise Estimation

In the current IceCube supernova analysis, the summed rates of all 5160 DOMs are used to identify supernova signals. If the same was done in PINGU with the configuration that was examined in this thesis, i. e. with $18 \cdot 350 = 6300$ DeepCore DOMs, the detection capabilities for supernovae could not be improved significantly as the total number of DOMs is only slightly increased. The higher quantum efficiency of the DeepCore PMTs is somewhat compensated by their higher noise rate. Since in PINGU the DOMs are much closer, one can reduce the background effectively by counting coincident hits[3].

Therefore one needs to find cuts for both time and spatial coincidence that decrease the noise rate as much as possible and limit the combinatorics, while leaving most of the actual signal untouched. In Figure 4.9 the distance as well as the time difference for the first two hits in each event with more than one hit are shown. The time distribution is, apart from a very sharp peak at differences close to zero, rather flat so that no obvious time cut comes to mind. Hence the spatial distances have to be considered first.

These do not drop significantly until about 40 m which would only allow for a rather weak cut. But the distribution has a very distinct structure. After dropping very rapidly, at 10 m a strong peak can be seen with a subsequent drop. At $\sim$ 17 m, 20 m, $\sim$ 26 m, ... similar features occur with decreasing prominence. As these numbers just match the distance of a given string to the nearest, next-to-nearest,

[3]Note that the significance is proportional to signal/$\sqrt{\text{background}}$, so a drastic background reduction is required.

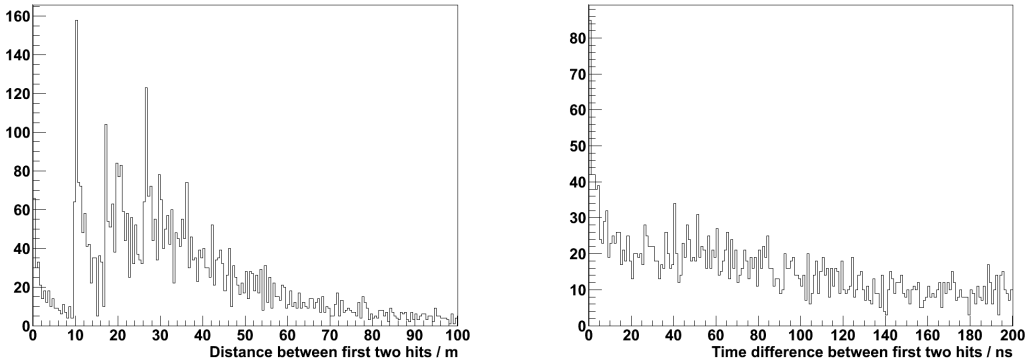

Figure 4.9: Spatial (left) and time (right) difference of multiple hits in a PINGU configuration with 10 m string and 1 m DOM spacing. For coincidences with three or more hits, only the first two were considered.

and so on, string, this structure indicates that a large fraction of the coincident hits does only have a small vertical distance while the horizontal distance can be quite large.

This can in fact be seen in Figure 4.10 left, where only the vertical distance between coincident hits is shown. The distribution has a much steeper slope than the one of the absolute hit distances and has no secondary structure, hence the peaks in Figure 4.9 left are in fact artefacts of the detector geometry.

A reasonable spatial cut for double coincidences can be applied at a vertical distance of 20 m, preserving 52 % of the signal. After this, a time cut with a coincidence window of 100 ns reduces the remaining number of hits further, so that a total of 31 % of the incoming signal remains after both cuts that correspond to the framed area in figure 4.10 right. In the future the cuts will be further optimised.

For triple coincidences, the cut values are chosen in a way that they are consistent with those for double coincidences. The time window is kept at 100 ns while the spatial cut requires the three hits to be within 40 m in vertical direction. By this choice, 23 % of the initial triple hits are preserved.

Now that the cuts have been specified, the noise rates that are to be expected from these values need to be estimated. These rates are made up of two different parts: The random noise that comes from the DOMs' dark noise rates of 720 Hz that lead to accidental coincidences between different DOMs and correlated noise from external sources, mostly atmospheric muons.

Although the latter do only cause a mean rate enhancement of ~ 22 Hz per DOM, they can have a strong impact in terms of supernova detection since they come in

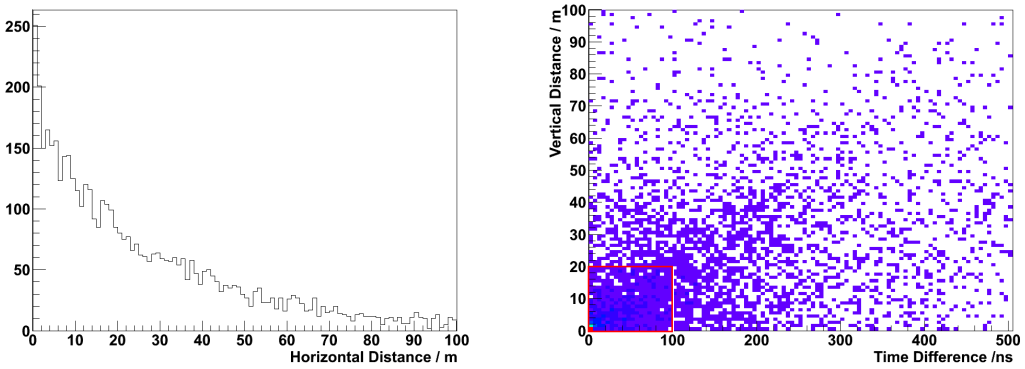

Figure 4.10: *Left:* Vertical distance of coincident hits.
Right: Spatial vs. time difference of coincident hits. The box represents the applied cuts.

bundles that can mimic the collective rate increase seen in case of a supernova and do also produce locally coincident hits [11]. As a large fraction of the atmospheric muons is triggered by IceCube, their rates can be subtracted afterwards from the supernova signal, reducing the number of contributing muons by about 50 % in the current IceCube analysis. By this, their influence on the significance can almost completely be suppressed. As PINGU will be located completely inside IceCube, the latter can be used as on-line veto for PINGU very effectively, so that muon-induced background should almost completely be discarded.

The random noise has a Poisson distribution and can be calculated accordingly. So for a single DOM the probability to see at least one random noise hit during a given coincidence window of $t_{\text{coinc}} = 100\,\text{ns}$ when its noise rate is $f_{\text{random}} = 720\,\text{Hz} \cdot 50\,\% = 360\,\text{Hz}$[4] is complementary to the probability to register no hit under the specified coincidence conditions and hence given by

$$p = 1 - \frac{\lambda^k}{k!} e^{-\lambda} \quad , \tag{4.2}$$

with $k = 0$ and λ being the expectation value of noise counts, given by

$$\lambda = f_{\text{random}} \cdot t_{\text{coinc}} = 3.60 \cdot 10^{-5} \quad . \tag{4.3}$$

For a random coincidence of at least two noise hits two independent DOMs that are within 20 m in vertical direction have to be triggered in this 100 ns. The probability

[4]The reduction by 50 % is due to the application of an artificial dead time.

of this has to be calculated according to a binomial distribution, again via the complementary probability of registering no or one noise hit:

$$\begin{aligned} P_{\text{double}} &= 1 - B(\,0\,|\,p, N_{\text{DOMs}}) - B(\,1\,|\,p, N_{\text{DOMs}}) \\ &= 1 - (1-p)^{N_{\text{DOMs}}} \cdot \left(1 + \frac{N_{\text{DOMs}} \cdot p}{1-p}\right) \quad . \end{aligned} \tag{4.4}$$

N_{DOMs} is the number of DOMs allowed for coincidences by the vertical distance cut. Since all DOMs within a 20 m layer[5] on all 18 strings are available one obtains

$$N_{\text{DOMs}} = 18 \cdot 21 = 378 \quad . \tag{4.5}$$

Apart from boundary effects, the rate of random coincidences per DOM is then

$$f_{\text{double}} = \frac{P_{\text{double}}}{t_{\text{coinc}} \cdot N_{\text{DOMs}}} = \frac{9.15 \cdot 10^{-5}}{100\,\text{ns} \cdot 378} \approx 2.42\,\text{Hz} \quad . \tag{4.6}$$

The rate for random triple coincidences can be determined in an analogue way. The time coincidence window t_{coinc} stays the same, but now the three hits are required to be within 40 m, thus the number of available DOMs rises to

$$N_{\text{DOMs}} = 18 \cdot 41 = 738 \quad . \tag{4.7}$$

Then the rate is given by

$$\begin{aligned} f_{\text{triple}} &= \frac{1 - B(\,0\,|\,p, N_{\text{DOMs}}) - B(\,1\,|\,p, N_{\text{DOMs}}) - B(\,2\,|\,p, N_{\text{DOMs}})}{t_{\text{coinc}} \cdot N_{\text{DOMs}}} \\ &\approx \frac{3.05 \cdot 10^{-6}}{100\,\text{ns} \cdot 738} \approx 0.0413\,\text{Hz} \quad . \end{aligned} \tag{4.8}$$

The standard deviation of these noise rates depends on the bin width in which the rates are counted and can be calculated according to

$$\sigma_{f_{\text{noise}}} = \frac{\sqrt{f_{\text{noise}} \cdot t_{\text{bin}}}}{t_{\text{bin}}} \quad . \tag{4.9}$$

For the standard analysis bin width of $t_{\text{bin}} = 500\,\text{ns}$ in IceCube, this leads to $\sigma_{f_{\text{double}}} = 2.2\,\text{Hz}$ and $\sigma_{f_{\text{triple}}} = 0.29\,\text{Hz}$ for the random double and triple coincidence rates.

These numbers can now be used to estimate an actual supernova signal in PINGU that can be compared to those of IceCube. These plots will give an idea on the improvements that can be achieved.

[5] Since both the topmost and lowermost DOM are assumed to be inside the layer this leads to a total of 21.

4.3 Supernova Detection in PINGU and IceCube

As IceCube already has a sufficient total active volume to trigger all galactic supernovae with high significance, the advantages of PINGU lie in improving the significance in the Magellanic Clouds and a better resolution of structures in the light curve.

To simulate the complete detector response of PINGU in case of a supernova, the Unified Supernova Simulation Routine (`USSR`) was used, a software that provides an estimate of the recorded count rates without actually tracking single events [37]. Although the `USSR` was designed to analyse the signatures of various supernova models in IceCube, it can easily be adopted for PINGU as all important detector parameters like active volumes, noise rates, and the number of DOMs can be adjusted to fit the new specifications.

4.3.1 Improving the Reach

The possible improvement in the reach for supernova detection is only a minor effect since IceCube already covers the complete Milky Way. However, the Large Magellanic Cloud, a satellite dwarf galaxy in approximately 50 kpc distance that has about 1 % of the Milky Way's mass, might be better accessible for PINGU. In Figure 4.11, signal estimates for a supernova in the Large Magellanic Cloud are shown. While in IceCube and in PINGU using double coincidences the signal is indiscernible from the detector noise, in the triple coincidence rate it is seen clearly as a rise in the coincidence rates and will be easy to trigger.

As the supernova model used in Fig. 4.11 is a rather weak one the fact that it is still visible implies that the reach for stronger models may be even further. This does not lead to much of an improvement in terms of the number of detectable supernovae, though, since the space beyond the Large Magellanic Cloud is nearly empty. The next larger accumulation of stars is the Andromeda Galaxy at a distance of about 760 kpc. This far away, conventional supernova models cannot be detected even with PINGU. A very extreme model, the direct collapse of a very massive progenitor into a black hole, produces a signal that is about half of the expected noise variation in a 500 ms binning (see Fig. 4.12) and might possibly be detectable if the signal-to-noise ratio could be improved, e. g. by tuning the coincidence cuts.

However, extending the reach to neighbouring galaxies will be one of the primary goals for PINGU phase 2 [36]. Although not being able to record detailed neutrino light curves from single extragalactic supernovae[6], the advance warnings that it will give for one to two supernovae in nearby galaxies per year will be extremely valuable for observing their optical signal from the very beginning, thus providing insights into supernova dynamics.

[6] On the other hand, one may "stack" several supernovae to learn about the characteristics of an ensemble of average supernovae.

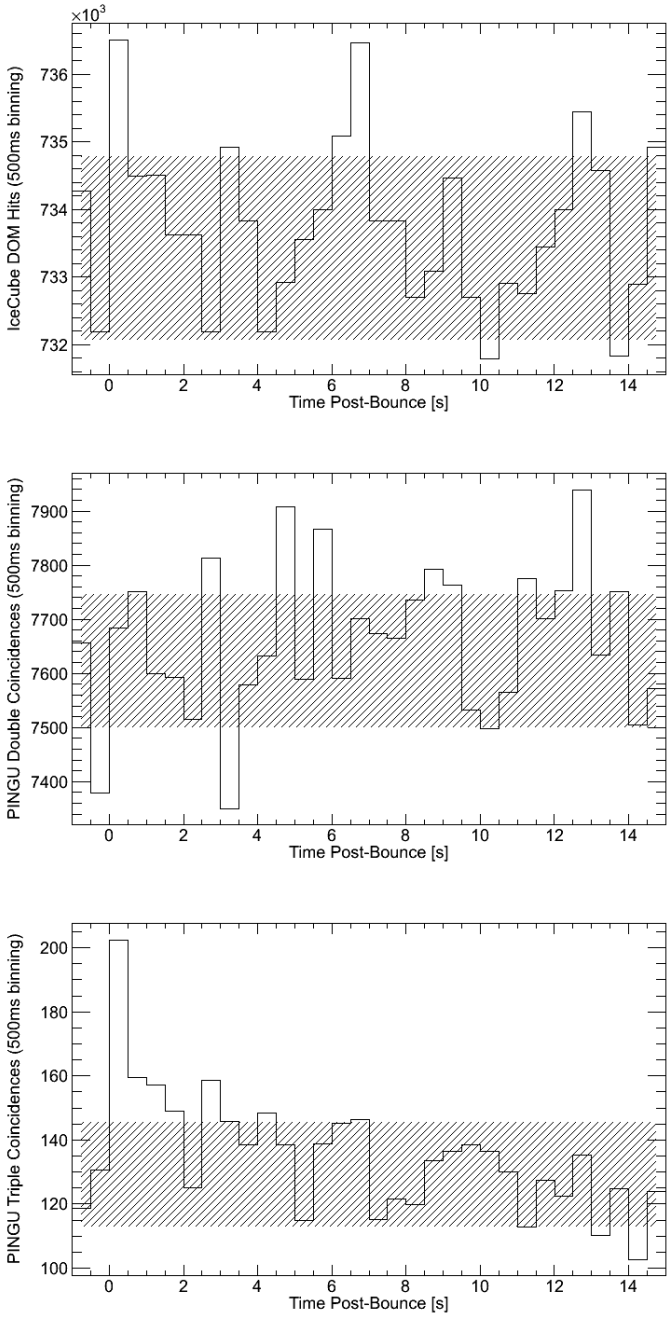

Figure 4.11: Expected detector response for a 8.8 $M_{\odot}$ progenitor mass supernova [28] in the Large Magellanic Cloud for the current IceCube setup (top), and PINGU using double (middle) and triple (bottom) coincidences. The shaded area denotes the noise level.

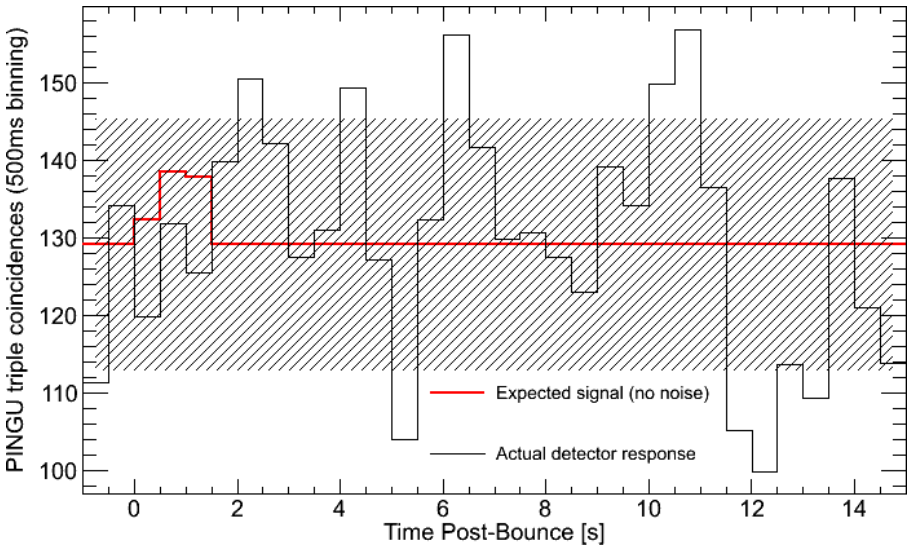

Figure 4.12: Signal expectation of a supernova in the Andromeda Galaxy directly collapsing into a black hole [53].

4.3.2 Improving the Light Curve Resolution

In terms of gathering information about the processes occurring during the collapse of the stellar core it is important to record not only the initial outbreak of neutrinos, but also the more subtle structures of the light curve during the cooling phase.

In the light curve's details there are artefacts of the dynamics governing the collapse of the stellar core closely entangled with intrinsic neutrino properties, especially oscillation parameters. To identify their effects separately requires a very detailed record of the light curve. From Figure 4.13 one can see that IceCube cannot sufficiently provide this, even though a rather extreme oscillation scenario was assumed that strengthens the differences between the models of the supernova's interior. For PINGU, however, the models can clearly be separated.

As a caveat one has to state that the interdependence of oscillation parameters and star matter effects are very delicate so that an external measurement of the former would be helpful for putting constraints on the models of the stellar interior. If the neutrino oscillations are well understood, a galactic supernova observed with PINGU will give a good image of the core collapse that will be able to distinguish between the supernova models currently on the market.

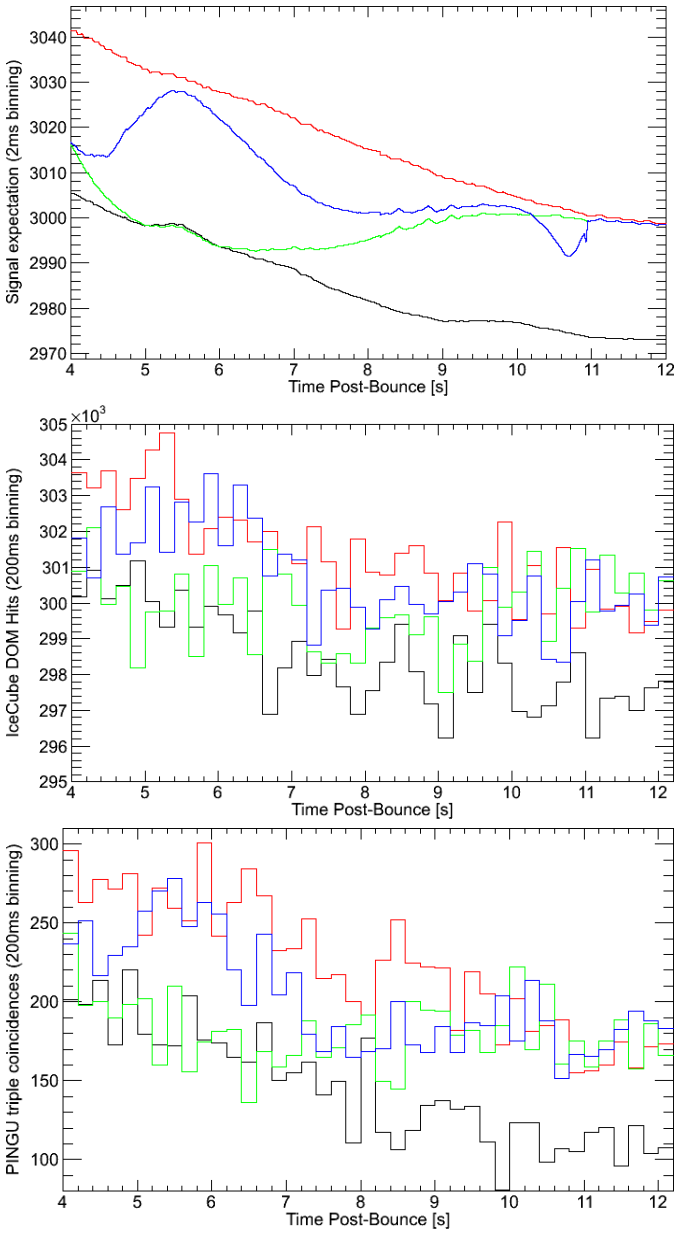

Figure 4.13: Comparison of different neutrino oscillation scenarios for a 20 $M_{\odot}$ progenitor mass supernova [56] in the galactic centre. Black denotes the signal without neutrino oscillations, while in red, green, and blue the effects of oscillations in a static density profile, with a forward, and with a forward and reverse shock front, respectively, are taken into account. Shown are the pure signal expectation (top), current IceCube (middle), and PINGU using triple coincidences (bottom). An inverted neutrino hierarchy with large mixing angle was assumed.

5 Conclusion

In this work, a `Geant4` based Monte Carlo simulation was developed to analyse the prospects of a low-energy extension to the IceCube neutrino telescope, called PINGU, for the detection of supernovae.

In the simulation that was named `I3_Sim`, the use of current technology of the DeepCore subdetector was implemented, including the depth-dependence of scattering and absorption in the polar ice. The detector geometry itself was left flexible, so that the configuration can be varied easily.

After cross-checking the output of `I3_Sim` with the expectations, its configuration was optimised for the detection of supernova neutrinos via double and triple coincident photon hits on different DOMs. Favoured by this analysis was a configuration with a spacing of 10 m between the 18 strings of the first deployment phase of PINGU, with the DOMs spaced by 1 m on the strings. The active volume per DOM in this set-up is $119 \pm 2\,\mathrm{m}^3$ for double and $47.8 \pm 1.0\,\mathrm{m}^3$ for triple coincidences. After applying cuts of a 100 ns coincidence window and the hits being within 20 m for double and 40 m for triple coincidences, 31 % and 23 %, respectively, of the active volume are left.

With this configuration, the possibilities of extracting additional information to the absolute neutrino light curve were examined, covering the observation of the mean neutrino energy and the reconstruction of the supernova direction. As both manifest in changing the relative rates of coincident and total hits and need an absolute normalisation, disentangling them is a delicate task. It might be possible, however, since the observation of a galactic supernova would provide vast statistics and hence very small errors on the count rates.

When comparing the capabilities of PINGU with those of IceCube, it was found that PINGU will extend the reach for supernova detection beyond the Magellanic Clouds and possibly be able to register a very extreme core-collapse even in the Andromeda Galaxy, if the random background can be reduced further. Also, it will provide a much better resolution of the neutrino light curve of galactic supernovae, thus being able to distinguish better between different neutrino oscillation scenarios.

In the future, the signal-to-noise ratio for coincidences can be improved by an optimisation of the coincidence windows, which were only chosen after a non-exhaustive analysis of their effect on the noise rates and the signal loss. Also, the influence of correlated noise especially from atmospheric muons has to be examined as these can produce a strong background signal, particularly when searching for coincident signals in different DOMs.

Especially when aiming towards extragalactic supernovae, the occurrence of very high multiplicity coincidences with more than five triggered DOMs, which means the transition from a rate-based to an event-based analysis, should be studied since they allow for a very effective reduction of background noise. Running both analyses in parallel would then provide both the clean recording of light curves of galactic supernovae via counting high rates of low multiplicity coincidences and the detection of very distant supernovae, where the light curve is not accessible in any case, by registering few high multiplicity coincidences.

Bibliography

[1] IAU Circular No. 4317.

[2] IceCube Gallery. `https://gallery.icecube.wisc.edu/internal/main.php`.

[3] *Physics Reference Manual*, 9.4 edition, December 2010.

[4] R. Abbasi et al. Calibration and characterization of the IceCube photomultiplier tube. *Nuclear Instruments and Methods in Physics Research Section A: Accelerators, Spectrometers, Detectors and Associated Equipment*, 618(1-3):139–152, 2010.

[5] R. Abbasi et al. IceCube Sensitivity for Low-Energy Neutrinos from Nearby Supernovae. *to be published*, 2011.

[6] M. Ackermann et al. Optical properties of deep glacial ice at the South Pole. *Journal of Geophysical Research*, 111(D13203), 2006.

[7] J. Ahrens et al. IceCube Preliminary Design Report. Technical Report 1.24, The IceCube Collaboration, October 2001.

[8] E. N. Alexeyev, L. N. Alexeyeva, I. V. Krivosheina, and V. I. Volchenko. Detection of the neutrino signal from SN 1987A in the LMC using the INR Baksan underground scintillation telescope. *Physics Letters B*, 205(2-3):209–214, 1988.

[9] P. Amram et al. Background light in potential sites for the ANTARES undersea neutrino telescope. *Astroparticle Physics*, 13(2-3):127–136, 2000.

[10] J. N. Bahcall et al. Standard neutrino spectrum from 8-B decay. *Physical Review C*, 54(1):411–422, July 1996.

[11] V. Baum et al. Supernova detection with IceCube and beyond. *Proceedings of the 32nd ICRC*, to be published.

[12] Vincent Bertin et al. Status and first results of the ANTARES neutrino telescope. *Nuclear Instruments and Methods in Physics Research Section A: Accelerators, Spectrometers, Detectors and Associated Equipment*, 604(1-2, Supplement 1):S136–S142, 2009. ARENA 2008.

[13] H. Bethe. Bremsformel für Elektronen relativistischer Geschwindigkeit. *Zeitschrift für Physik*, 76(5-6):293–299, 1932.

[14] R. M. Bionta et al. Observation of a neutrino burst in coincidence with supernova 1987A in the Large Magellanic Cloud. *Physical Review Letters*, 58(14):1494–1496, Apr 1987.

[15] E. M. Burbidge, G. R. Burbidge, W. A. Fowler, and F. Hoyle. Synthesis of the Elements in Stars. *Review of Modern Physics*, 29(4):547–650, Oct 1957.

[16] CERN. *ROOT Users Guide 5.26*, December 2009.

[17] S. Chandrasekhar. The Maximum Mass of Ideal White Dwarfs. *Astrophysical Journal*, 74:81–82, July 1931.

[18] D. Chirkin et al. Study of South Pole ice transparency with IceCube flashers. `http://icecube.wisc.edu/~dima/work/WISC/ppc/spice/paper/a.pdf`, March 2011.

[19] Hamamatsu Corporation. Hamamatsu R7081-02 data sheet.

[20] R. Davis, D. S. Hamer, and K. C. Hoffman. Search for Neutrinos from the Sun. *Physical Review Letters*, 20:1205–1209, May 1968.

[21] BeyondDC DokuWiki. Geometry. `http://icecube.phys.ualberta.ca:8080/dokuwiki/doku.php?id=geometry`, November 2010.

[22] S. Fukuda et al. The Super-Kamiokande detector. *Nuclear Instruments and Methods in Physics Research Section A: Accelerators, Spectrometers, Detectors and Associated Equipment*, 501(2-3):418–462, 2003.

[23] Y. Fukuda et al. Evidence for Oscillation of Atmospheric Neutrinos. *Physical Review Letters*, 81:1562–1567, August 1998.

[24] T. Griesel. *Optimierung des Nachweises von Supernovae in IceCube.* PhD thesis, Universität Mainz, 2010.

[25] W. C. Haxton and R. G. H. Robertson. Solar neutrino interactions with 18-o in the SuperKamiokande water cerenkov detector. *Physical Review C*, 59(1):515–519, January 1999.

[26] L. G. Henyey and J. L. Greenstein. Diffuse radiation in the Galaxy. *Astrophysical Journal*, 93:70–83, 1941.

[27] K. Hirata et al. Observation of a neutrino burst from the supernova SN1987A. *Physical Review Letters*, 58(14):1490–1493, Apr 1987.

[28] L. Hüdepohl, B. Müller, H.-T. Janka, A. Marek, and G. G. Raffelt. Neutrino Signal of Electron-Capture Supernovae from Core Collapse to Cooling. *Phys. Rev. Lett.*, 104(25):251101, Jun 2010.

[29] P. O. Hulth. What have we learned about the hole ice from the Swedish cameras in string 80? PINGU workshop, March 2011.

[30] S. Hundertmark. *Simulation und Analyse von Myonereignissen im AMANDA-B4-Neutrinoteleskop*. PhD thesis, Humboldt-Universität zu Berlin, 1999.

[31] J. D. Jackson. *Klassische Elektrodynamik*. de Gruyter, 3rd edition, 2002.

[32] H.-Th. Janka, K. Langanke, A. Marek, G. Martínez-Pinedo, and B. Müller. Theory of core-collapse supernovae. *Physics Reports*, 442(1-6):38–74, April 2007.

[33] M.-Th. Keil, G. G. Raffelt, and H.-Th. Janka. Monte Carlo Study of Supernova Neutrino Spectra Formation. *Astrophysical Journal*, 590(2):971–991, June 2003.

[34] E. Kolbe, K. Langanke, and P. Vogel. Estimates of weak and electromagnetic nuclear decay signatures for neutrino reactions in Super-Kamiokande. *Physical Review D*, 66:013007, July 2002.

[35] K. Kotake, K. Sato, and K. Takahashi. Explosion mechanism, neutrino burst and gravitational wave in core-collapse supernovae. *Reports on Progress in Physics*, 69:971–1143, 2006.

[36] M. Kowalski, S. Böser, and N. Linn. PINGU Phase II - a X-megaton SN neutrino detector. PINGU workshop, March 2011.

[37] T. Kowarik. *Supernova Neutrinos in AMANDA and IceCube*. PhD thesis, Universität Mainz, 2010.

[38] J. Magill, G. Pfennig, and J. Galy. Karlsruher Nuklidkarte, November 2007.

[39] D. Malin. Before and after SN1987A. `http://www.aao.gov.au/images/captions/aat050.html`, August 2010.

[40] F. Mannucci, D. Maoz, K. Sharon, M. T. Botticella, M. Della Valle, A. Gal-Yam, and N. Panagia. The supernova rate in local galaxy clusters. *Monthly Notices of the Royal Astronomical Society*, 383(3):1121–1130, 2008.

[41] W. J. Marciano and Z. Parsa. Neutrino–electron scattering theory. *Journal of Physics G: Nuclear and Particle Physics*, 29(11):2629–2645, November 2003.

[42] A. Marek, H.-Th. Janka, and E. Müller. Equation-of-state dependent features in shock-oscillation modulated neutrino and gravitational-wave signals from supernovae. *Astronomy & Astrophysics*, 496(2):475–494, 2009.

[43] Gustav Mie. Beiträge zur Optik trüber Medien, speziell kolloidaler Metallösungen. *Annalen der Physik*, 330(3):377–445, 1908.

[44] K. Nakamura et al. 2010 Review of Particle Physics. *Journal of Physics G*, 37:075021, 2010.

[45] J. R. Oppenheimer and G. M. Volkoff. On Massive Neutron Cores. *Physical Review*, 55(4):374–381, Feb 1939.

[46] A. Piégsa. *Supernova-Detektion mit dem IceCube-Neutrinoteleskop*. PhD thesis, Universität Mainz, 2009.

[47] P. Podsiadlowski. The progenitor of SN 1987 A. *Publications of the Astronomical Society of the Pacific*, 104:717–729, September 1992.

[48] P. B. Price. Latest results from AMANDA. In Y. Giraud-Héraud and J. Thanh Van Tran, editors, *Phénomènes à très hautes énergies dans l'univers*, pages 255–260. Editions Frontieres, 1997.

[49] P. B. Price and L. Bergström. Optical properties of deep ice at the South Pole: scattering. *Applied Optics*, 36(18):4181–4194, Jun 1997.

[50] P. B. Price and K. Woschnagg. Role of group and phase velocity in high-energy neutrino observatories. *Astroparticle Physics*, 1:97–100, March 2001.

[51] C. E. Rolfs and W. S. Rodney. *Cauldrons in the Cosmos*. The University of Chicago Press, 1st edition, 1988.

[52] M. Salathe. Novel Search Methodology for Supernovae with IceCube. Master's thesis, Ecole Polytechnique Fédérale de Lausanne, February 2011.

[53] K. Sumiyoshi, S. Yamada, and H. Suzuki. Dynamics and neutrino signal of black hole formation in nonrotating failed supernovae. i. equation of state dependence. *Astrophysical Journal*, 667(1), September 2007.

[54] R. C. Tolman. Static Solutions of Einstein's Field Equations for Spheres of Fluid. *Physical Review*, 55(4):364–373, Feb 1939.

[55] R. Tomàs, D. Semikoz, G. G. Raffelt, M. Kachelrieß, and A. S. Dighe. Supernova pointing with low- and high-energy neutrino detectors. *Physical Review D*, 68:093013, November 2003.

[56] T. Totani, K. Sato, H. E. Dalhed, and J.R. Wilson. Future Detection of Supernova Neutrino Burst and Explosion Mechanism. *Astrophysical Journal*, 496(1), March 1998.

[57] F. Vissani and A. Strumia. Precise quasielastic neutrino/nucleon cross-section. *Physics Letters B*, 564:42–54, 2003.

[58] P. Vogel and J. F. Beacom. Angular distribution of neutron inverse beta decay. *Physical Review D*, 60:053003, 1999.

[59] C. Wiebusch. Physics Capabilities of the IceCube DeepCore Detector. *Proceedings of the 31st ICRC*, July 2009.

[60] IceCube Wiki. DOM Acceptance Table for Photonics and Romeo. `http://wiki.icecube.wisc.edu/index.php/DOM_Acceptance_Table_for_Photonics_and_Romeo`, March 2010.

Selbstständigkeitserklärung

Hiermit versichere ich, die vorliegende Arbeit selbstständig und unter ausschließlicher Verwendung der angegebenen Literatur und Hilfsmittel erstellt zu haben.

Die Arbeit wurde bisher in gleicher oder ähnlicher Form weder veröffentlicht noch einer anderen Prüfungsbehörde vorgelegt.

Mainz, den 14. Juni 2011

Danksagung

Aus datenschutzrechtlichen Gründen gelöscht.